Aerospace Science and Technology 142 (2023) 108700

Contents lists available at ScienceDirect

Aerospace Science and Technology

journal homepage: www.elsevier.com/locate/aescte

Design optimisation of non-axisymmetric exhausts for installed civil aero-engines

J. Hueso-Rebassa [a,*], D. MacManus [a], F. Tejero [a], I. Goulos [a], F. Sánchez-Moreno [a], C. Sheaf [b]

[a] Centre for Propulsion and Thermal Power Engineering, Cranfield University, Bedfordshire, MK43 0 AL, United Kingdom
[b] Rolls-Royce plc, P.O Box 31, Derby, DE24 8BJ, United Kingdom

ARTICLE INFO

Communicated by Mehdi Ghoreyshi

ABSTRACT

Future civil aero-engines are likely to operate with higher bypass-ratios (BPR) than current power-plants to improve propulsive efficiency and reduce specific thrust. This will probably be accompanied by an increase of fan diameter and size of the power plant. Consequently, future configurations are likely to require more close-coupled installations with the airframe due to structural and ground clearance requirements. This tendency may lead to an increase in the adverse installation effects which could be mitigated with non-axisymmetric exhausts. However, due to the prohibitive computational cost, limited regions of the design space have been studied. For this reason, a relatively low-cost design approach for the integrated system is required. The aim of this work is to establish a method to map the non-axisymmetric exhaust design space where the effects of the propulsion system installation are taken into account. The methodology relies on the generation of a design database using inviscid computational fluid dynamics (CFD) methods. This is used to characterise the design space, identify the dominant design parameters and build response surface models for optimisation. The candidate designs that arise from the optimisation are assessed with viscous CFD simulations to assess the aerodynamic mechanisms and performance characteristics. The result is a set of design recommendations for installed configurations with non-axisymmetric exhausts. The method is an enabler for the optimisation of installed propulsion systems and has provided an exhaust design with a 0.7% improvement on net vehicle force relative to an axisymmetric exhaust, for a close coupled configuration where the fan cowl is overlapped with the wing. A reduction in net vehicle force is expected to lead to a similar reduction in cruise fuel burn.

1. Introduction

1.1. Background

Future civil aero-engines are likely to operate with higher bypass-ratios (BPR) [1] and lower fan pressure ratios than current power-plants to improve propulsive efficiency and reduce specific thrust [2]. This will be accompanied by an increase of fan diameter and size of the power plant and nacelle. Consequently, for podded under-wing configurations of Ultra-High Bypass Ratio (UHBR) aero-engines, the integration of the propulsion system with the airframe requires careful consideration. UHBR engines are expected to be installed in a more close coupled arrangement with the wing to meet ground clearance requirements [3]. However, for such installations, the aerodynamic engine-airframe interactions could have a detrimental impact on the performance, aeroelasticity and aeroacoustics of both the airframe and engine [4]. Moreover, it could alter the working conditions of the engine turbomachinery [5].

The engine-airframe aerodynamic interference is characterised by a flow over-acceleration and a shock wave at the nacelle inboard side. This is related to a channelling effect produced by the geometric integration of the nacelle, wing, pylon, exhaust jet and fuselage [6,7]. In close coupled configurations, the aerodynamic effects of propulsion system installation could penalise the aircraft net vehicle force (NVF) by 0.7% of the standard nominal thrust (F_N) relative to a more conventional installation position [6]. This is partly related to a reduction of the exhaust system performance. The Gross Propulsive Force (GPF)

* Corresponding author.
E-mail address: j.hueso-rebassa@cranfield.ac.uk (J. Hueso-Rebassa).

https://doi.org/10.1016/j.ast.2023.108700
Received 19 July 2023; Received in revised form 2 October 2023; Accepted 24 October 2023
Available online 27 October 2023
1270-9638/© 2023 The Authors. Published by Elsevier Masson SAS. This is an open access article under the CC BY license (http://creativecommons.org/licenses/by/4.0/).

Nomenclature

Abbreviations

$CNPR$	Core Nozzle Pessure Ratio = $P_{inlet}^{CR}/p_{\infty}$
DOE and DSE	Design Of Experiment and Design Space Exploration
DOF	Degree of Freedom
$FNPR$	Fan Nozzle Pessure Ratio = $P_{inlet}^{BP}/p_{\infty}$
GA	Genetic Algorithm
GPF	Gross Propulsive Force ..... [N]
LHS	Latin Hypercube Sampling
$MFCR$	Mass Flow Capture Ratio = A_{∞}/A_{hl}
NPF	Net Propulsive Force ..... [N]
NVF	Net Vehicle Force ..... [N]
RSM	Response Surface Model
$UHBR$	Ultra High Bypass Ratio

Greek Symbols

δ_{DL} and δ_{DS}	Vertical and lateral thrust vector angles ..... [rad]
μ	Dynamic viscosity..... [Pa s]
ϕ_{pitch}	Installation pitch angle ..... [rad]
ϕ_{toe}	Installation toe angle ..... [rad]
ψ	Azimuthal coordinate..... [rad]
ρ	Flow density..... [kg/m^3]

Roman Symbols

$\dot{m}$	Mass flow rate..... [kg/s]
$\hat{i}_x^{A/F}$, $\hat{i}_y^{A/F}$, $\hat{i}_z^{A/F}$	Airframe axes reference frame unit vectors
$\hat{i}_x^{Eng}$, $\hat{i}_y^{Eng}$, $\hat{i}_z^{Eng}$	Engine axes reference frame unit vectors
$\hat{i}_D$,$\hat{i}_S$,$\hat{i}_L$	Aerodynamic axes reference frame unit vectors
C_L and C_D	Lift and drag Coefficient
C_{ref} and A_{ref}	Reference chord length and area..... [m and m^2]
C_v and C_d	Velocity and discharge coefficients
dX and dZ	Nacelle trailing edge axial and vertical offset from wing leading edge..... [m]
F_N	Standard nominal net thrust..... [N]
F_{G0}	Intake momentum..... [N]
$L_{A/F}$ and $D_{A/F}$	Airframe lift and drag..... [N]
L_{nac}^* and D_{nac}^*	Modified nacelle lift and drag..... [N]
P and T	Stagnation pressure and temperature..... [Pa and K]
p and t	Static pressure and temperature..... [Pa and K]
q	Dynamic pressure ..... [Pa]
y^+	Non-dimensional wall distance
M and Re	Mach and Reynolds numbers

Subscripts and superscripts

*	Modified metric definition
$_{BP}$ and $_{CR}$	Referring to the bypass and core nozzles
$_{\infty}$ and $_{is}$	Referring to free-stream and isentropic conditions
$_{\delta_{DL}}$ and $_{\delta_{DS}}$	Referring to vertical and lateral thrust vectoring components of the propulsive force
$_{A/C}$ and $_{A/F}$	Referring to the whole aircraft and airframe only
$_{mag}$ and $_{vect}$	Referring to magnitude and vectoring components of the propulsive force

could be reduced by approximately 2.0% of the engine nominal thrust relative to conventional installation positions [6] while the nacelle drag could increase by about 2.0% [7].

1.2. Non-axisymmetric exhaust systems for propulsion integration

An improved integration of UHBR engines with the airframe could be achieved with non-axisymmetric exhaust systems. Non-axisymmetric configurations of the exhaust typically involve scarfed [8,9] and non-circular designs of the bypass or core nozzles [10–12]. Otter et al. [10,11] developed a fully parametric approach for the design of non-axisymmetric exhausts. The method was based on intuitive Class Shape Transformation functions (iCSTs) [13–15] and was applied to design bypass nozzles with perturbations of the trailing edge radius. Once installed, these configurations mitigated the aerodynamic interference between the airframe and power plant and reduced the fuel consumption by $\approx 0.6\%$ relative to an equivalent axisymmetric configuration [11]. A different parametric design approach was investigated by Hueso-Rebassa et al. [8]. The study considered azimuthal perturbations of the longitudinal position of the bypass trailing edge. This parametrisation could benefit the NVF by up to 0.4% of the nominal thrust relative to the axisymmetric exhaust baseline. Bagy et al. [16] proposed an alternative design method for non-axisymmetric exhausts. The framework used detailed computed aided design (CAD) and a dimensionality reduction approach. Although the methodology proved useful for fine tuning of an industrial geometry, it lacked the geometric control of a parametric approach which is required to study the design space in early stages of the design process.

Although the previous research [8,10,11,16] set the basis for non-axisymmetric exhaust design, it was limited to a few configurations of the bypass nozzle and afterbody that were assessed independently. Moreover, these studies did not consider the effects of engine-airframe integration in the design process. Therefore, there is a need to develop design and optimisation methods for exhausts systems that account for the effects of engine-aircraft integration.

1.3. Design space exploration and optimisation of engine housing components

One of the main challenges of aerodynamic design is the large number of design variables considered during the process. This aspect, combined with the computational time required by CFD computations, limits the design capabilities. Although computing power continuously grows, conventional design methods based Reynolds Averaged Navier-Stokes (RANS) CFD makes the computational cost prohibitive, within an industrial context, for the exploration and optimisation of large-dimensional complex design spaces. Therefore, lower-cost design methodologies are required. For these reasons, design space exploration (DSE) and optimisation methods can be combined with lower-order CFD methodologies and Response Surface Models (RSM).

Data driven methods and machine learning techniques such as Kriging [17,18] and Artificial Neural Networks [19,20] (ANN) can approximate the response of the non-linear system and be used as surrogate models in the optimisation process. This could reduce significantly the computational cost of the optimisation [21]. Different methodologies for the design of propulsion system configurations were built upon RSMs. These include optimisation for preliminary engine design [22], nacelle geometries [23–25] and separate-jet exhaust systems [26,27]. Goulos et al. [26,27] developed an integrated methodology for the design space exploration (DSE) and optimisation of exhaust systems. The methodology was based on Kriging RSMs [17,18] constructed with CFD data of two-dimensional axisymmetric separate-jet exhausts. The resultant RSM was used to drive a genetic algorithm (GA) optimisation. The methodology targeted the optimisation of conventional and novel UHBR exhaust systems and lead to net propulsive force (NPF) benefits of 3.4% and 1.4% respectively [26], relative to baseline configurations. Magrini et al. [25] developed a multi-level optimisation approach for nacelles. The method started with a multi-objective CFD in-the-loop optimisation for 2D axisymmetric nacelle geometries, similar to other work [23,24]. The candidate designs were then optimised in three dimensions with a pylon through an RSM based approach. The

final configurations were evaluated installed with the airframe. Therefore, the effects of propulsion system integration were not considered in the optimisation process.

For installed configurations of propulsion systems, even the acquisition of sufficient data to build reliable surrogate models is infeasible. For this reason, Euler based CFD methods may provide a viable alternative. These methods could approximate the aerodynamics of installed propulsion systems at a fraction of the computational cost relative to a method based on Reynolds-Averaged Navier-Stokes (RANS) equations [28]. This may allow wider and more thorough explorations of the design space and may enable the acquisition of sufficient reliable data to formulate accurate prediction models. Ronzheimer et al. [29] proposed an Euler CFD based optimisation method for the integration of tail-mounted nacelles of business jets. The method targeted the optimisation of the tail cone of the aircraft in the presence of a nacelle and a pylon. The optimisation significantly mitigated the aerodynamic integration effects and reduced the aircraft drag by 2.5 drag counts relative to a baseline. However, no viscous CFD solutions were reported. Sanchez-Moreno et al. [30] developed an optimisation for installed configurations of UHBR non-axisymmetric nacelles. The method was based on Kriging RSMs and Euler CFD to sample the design space. After a genetic optimisation, the optimum design was assessed with RANS CFD. The method identified nacelle configurations that improved the aircraft NVF by $0.006F_N$, relative to the baseline design. The methodology reduced the computational cost by a factor of thirty-six relative to an equivalent optimisation with RANS CFD. This enabled the use of Euler CFD and RSM based optimisation for installed configurations of the propulsion system. However, this study did not consider the optimisation of the exhaust system.

There is a clear need to design compact non-axisymmetric nacelles and non-axisymmetric exhaust systems to retain the benefits from the new engine cycles once the propulsion system is installed. Whilst there have been several investigations on the design optimisation of non-axisymmetric nacelles coupled with the airframe [29,30], most of the research on exhaust optimisation was limited to axisymmetric geometries where the effects of propulsion system integration were not considered [26,27].

1.4. Scope of the present work

Relative to previous research on axisymmetric [26,27,31,32] and non-axisymmetric [8,10,11] exhaust systems, this work develops a methodology for the design and optimisation of aero-engine exhausts including the effects of propulsion integration. The novelty of this research is the characterisation of the design space of UHBR non-axisymmetric exhausts considering the effects of the installation of the propulsion system. This includes the identification of the dominant design parameters, the effect of design constraints, an analysis of the aerodynamic mechanisms and the optimisation of installed exhaust configurations. The contribution is a relatively low-cost design optimisation approach for installed UHBR aero-engines. In addition, the analysis of the underlying aerodynamics revealed thrust vectoring mechanisms by which non-axisymmetric exhausts improve the aircraft performance. The impact of the work is the potential fuel burn benefits of optimised non-axisymmetric configurations. The proposed method has identified exhaust designs with an improvement in net vehicle force of about 0.7% of cruise net thrust (F_N) relative to an axisymmetric exhaust for a close coupled configuration. A reduction in net vehicle force is expected to lead to a similar reduction in cruise fuel burn.

Overall, the structure of this work includes a detailed description of the design methodology and its application to study and optimise installed non-axisymmetric exhausts. The method encompasses the parametrisation of three-dimensional exhaust systems, the integration of the exhaust with the propulsion system and airframe, the computational assessment of the resultant configurations and design approaches such as design space exploration, response surface modelling and optimisation. The method is applied to survey the design space and to optimise installed non-axisymmetric exhausts.

2. Methodology

The design of non-axisymmtric separate-jet exhausts for installed UHBR configurations encompasses the parametrisation of three-dimensional exhausts geometries, the installation of the powerplant with the airframe and the assessment of the complete engine-airframe system with CFD. The methodology is integrated with design space exploration, response surface modelling and optimisation routines to evaluate the design space and identify candidate configurations that may improve the overall aircraft net vehicle force.

2.1. Baseline propulsion system and installation

The baseline propulsion system is a modern Ultra High Bypass Ratio (UHBR) engine with bypass ratio of $BPR = \dot{m}^{BP}/\dot{m}^{CR} > 15$ [6] and a standard nominal thrust of $60kN$ ($F_N \approx 60kN$) [6]. The propulsion system is configured with an axisymmetric exhaust and a non-axisymmetric nacelle. The nacelle is compact with $L_{nac}/R_{hi} = 3.1$ and $R_{TE}/R_{hi} = 0.91$ [23,24] (Fig. 1a). It was optimised by Tejero et al. [23,24] using a methodology based on uninstalled, three-dimensional configurations. The reference axisymmetric exhaust is a separate-jet configuration and it was optimised with a method based on 2D axisymmetric geometries by Goulos et al. (Fig. 1b) [26].

The powerplant is installed under-wing of the high-speed NASA Common Research Model (CRM) [33–35] with a pylon (Fig. 1c). The propulsion system is installed with the same pitch ($\phi_{pitch} = 1.75^o$) and toe ($\phi_{toe} = 2.25^o$) angles as the benchmark CRM with a through-flow nacelle [36] (Fig. 2a). At a fixed span-wise location along the wing, the installation position is defined as the offset between the wing leading edge and the nacelle trailing edge at the top aeroline (Fig. 2). The horizontal (dX/C_{ref}) and vertical (dZ/C_{ref}) components of the position are normalised with the wing chord ($C_{ref} = 7.8m$ [35]) of the local airfoil at the target span-wise location. This work focuses on a closely coupled installation position representative of future UHBR engines. In this arrangement, the nacelle is overlapped with the wing ($dX/C_{ref} = 0.03$, $dZ/C_{ref} = 0.075$, Fig. 2b) [6]. For non-axisymmetric configurations of the exhaust, the axial position and radius of the bypass trailing edge may vary azimuthally relative to the baseline. For this reason, the installation position is always referenced to the axisymmetric equivalent configuration.

The operating conditions of interest are of a typical mid-cruise segment of a long range flight (Table 1). These include a cruise altitude of $h = 10668m$, a flight Mach number of $M_\infty = 0.85$ and a Reynolds number based on the reference chord of $Re_{C_{ref}} = 46 \times 10^6$. The International Standard Atmosphere (ISA) model [37] was used to calculate the ambient conditions of static pressure (p_∞) static temperature (t_∞) and density (ρ_∞) at the cruise altitude. The engine cycle is based on published information [6]. The intake is designed for a Mass Flow Capture Ratio of $MFCR = A_{hi}/A_\infty \approx 0.7$ and the exhaust system is sized for a Fan Nozzle Pressure Ratio of $FNPR = P^{BP}_{inlet}/p_\infty \approx 2.2$ and a Core Nozzle Pressure Ratio of $CNPR = P^{CR}_{inlet}/p_\infty \approx 1.5$ [6]. These values were calculated by Goulos et al. [6,38] on the basis of minimising Specific Fuel Consumption (SFC) at mid-cruise conditions.

2.2. Geometry parametrisation of non-axisymmetric exhaust systems

Three-dimensional geometries of the propulsion system were generated from different aero-lines across the azimuthal range (ψ, Fig. 1b). Each aero-line is developed with intuitive Class Shape Transformation (iCST) functions [13–15]. These allow geometries of fan cowls [15,24], intakes [15], exhausts [38] and pylons [11] to be characterised by intuitive geometric parameters. The parametrisation of axisymmetric exhaust systems was extended to non-axisymmetric geometries by the

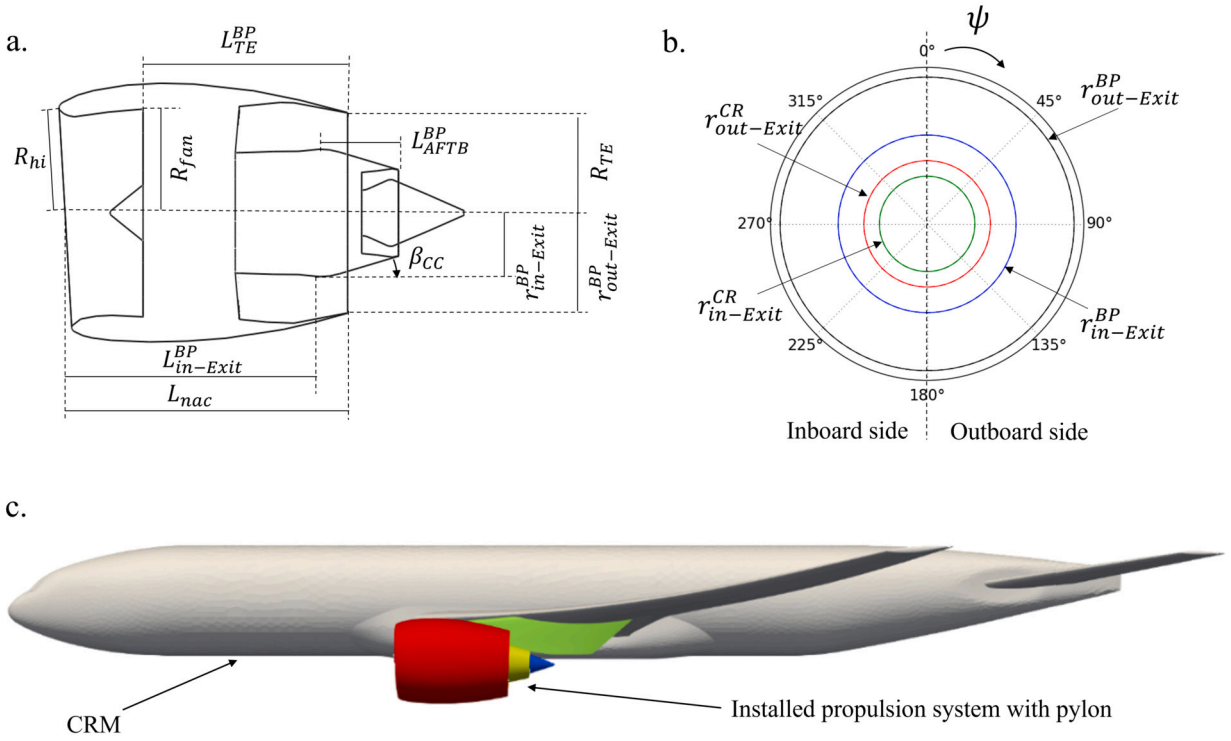


Fig. 1. Baseline propulsion system configuration with (a) side and (b) nozzle views. (c) Schematic of a propulsion system installed with the CRM.

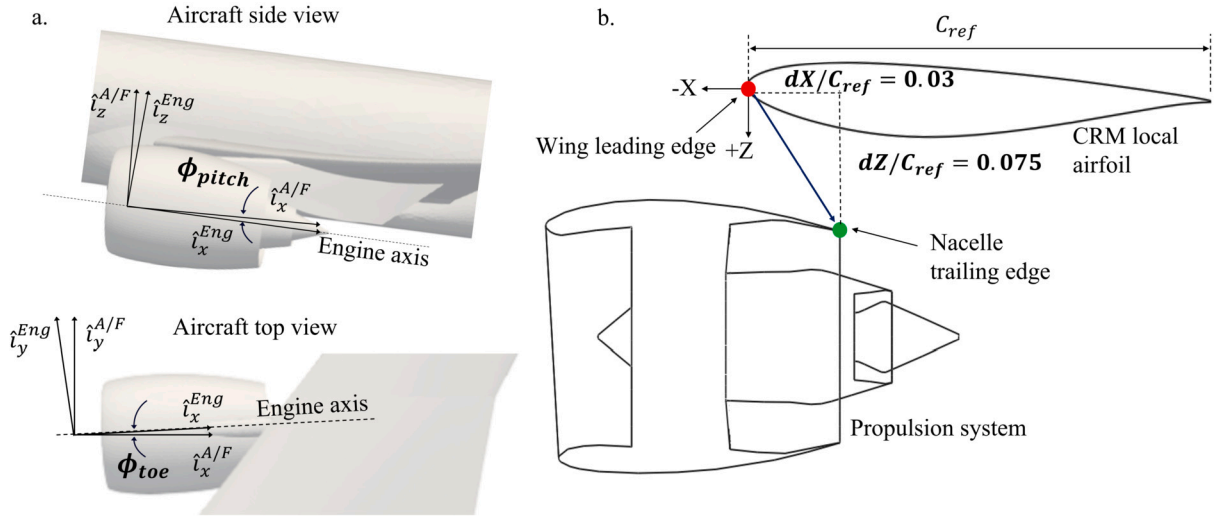


Fig. 2. (a) Definition of pitch (top) and toe (bottom) installation angles and (b) definition of the baseline installation position [6].

Table 1
Summary of the cycle parameters of the propulsion system and operating conditions of the CRM at mid cruise conditions [6].

Engine cycle parameter	value	CRM operating conditions	value
Bypass ratio	> 15	h	10668 m
Standard net thrust	≈ 60kN	M_∞	0.85
MFCR	≈ 0.7	$Re_{C_{ref}}$	45×10^6
FNPR	≈ 2.2		
CNPR	≈ 1.5		

addition of azimuthal iCSTs that modify the constrained points of each aero-line azimuthally [10,11]. This work focuses on azimuthal perturbations that modify the axial position and radius of the bypass trailing edge relative to the baseline configuration with an axisymmetric exhaust.

The perturbation of the axial position of the bypass trailing edge (L_{TE}^{BP}) [8], also called shear, is a particular case of nozzle scarfing [9] where only the axial component of the transformation is applied. The transformation produces an azimuthal distribution of L_{TE}^{BP} ($L_{TE}^{BP} = f(\psi)$, Fig. 3). The shear perturbation is defined terms of a shear angle (θ_A) and the azimuthal position of maximum L_{TE}^{BP} (ψ_A, Fig. 3a). With ψ_A, the perturbation can be applied around any rotation axis throughout the azimuth. The shear perturbation is expressed as in equation (1).

$$L_{TE}^{BP}/L_{TE_{ref}}^{BP}(\psi) = (1 + sin(\theta_A))cos(\psi - \psi_A) \quad (1)$$

When the bypass nozzle is sheared, the after-body can no longer remain axisymmetric. The variation of the bypass exhaust length at the outer aerolines propagates to the inner aerolines (Fig. 3b). At a single azimuthal position, the inner point of the bypass exit plane is similarly displaced axially. In addition, to maintain an axisymmetric core nozzle,

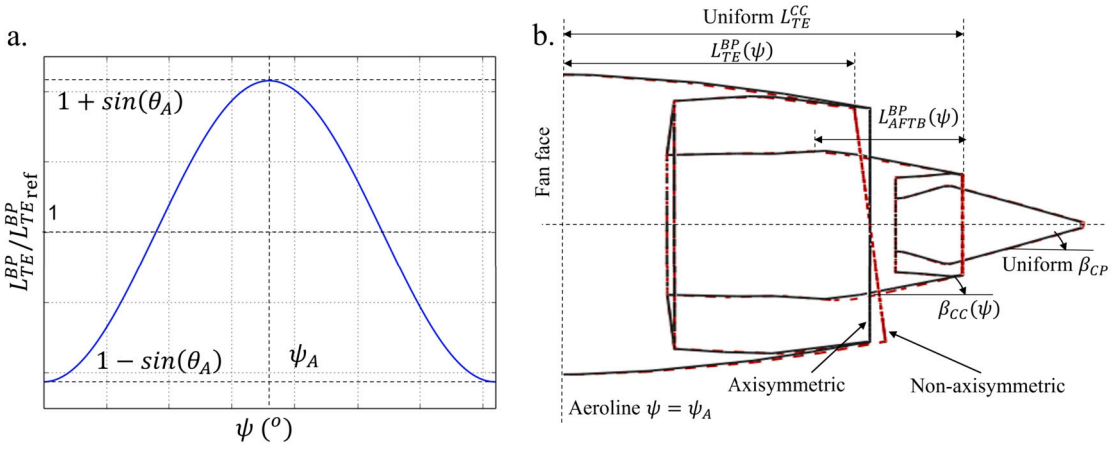


Fig. 3. Definition of the shear perturbation of the bypass trailing edge. (a) Distribution of L_{TE}^{BP} and (b) after-body control.

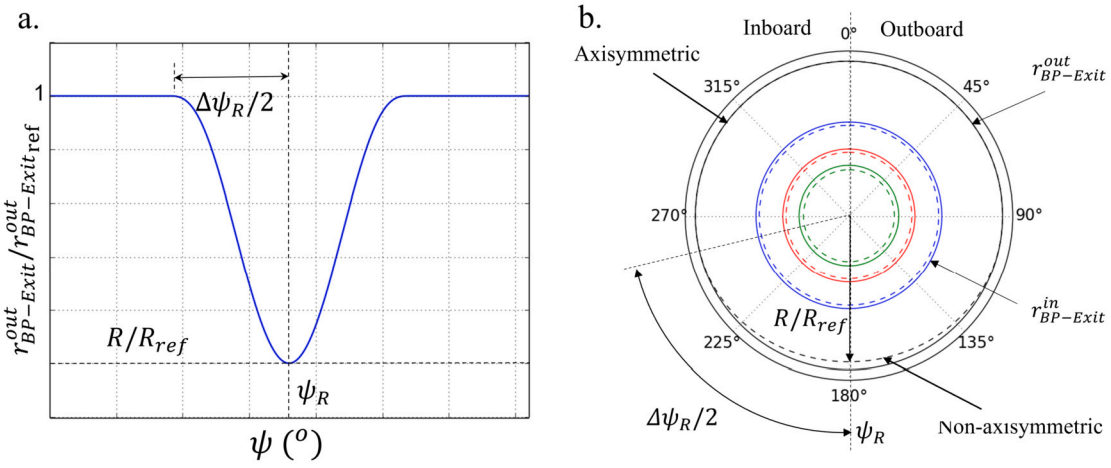


Fig. 4. Definition of the perturbation of the bypass trailing edge radius. (a) Distribution of $r_{BP-Exit}^{out}$ and (b) bypass exit area control.

the core cowl trailing edge is kept at a constant axial position across the annulus (Fig. 3b). However, as the position of the bypass exit plane changes azimuthally, the core cowl boat tail angle (β_{cc}) and the bypass after-body length (L_{AFTB}^{BP}) also vary (Fig. 3b). The axial position of the core cowl trailing edge is controlled with the circumferentially averaged after-body length ($L_{AFTB}^{BP}/L_{AFTB_{ref}}^{BP}$).

The second family of perturbations is an azimuthal distribution of the fan cowl trailing edge radius ($r_{out-exit}^{BP}$) (Fig. 4). It is controlled by three degrees of freedom. These are the variation of the radius relative to the reference exhaust (R/R_{ref}), the azimuthal position where the modification is centred (ψ_R) and the azimuthal extend ($\Delta\psi_R$) (Fig. 4a). For an exhaust design, it is vital to achieve the required exit area to ensure that the engine mass flow can be achieved. Therefore, for a non-axisymmetric configuration where the fan cowl radius is varying, it is necessary to ensure that the required area is also maintained. This is accommodated by an azimuthally uniform change to the radius of the inner point of the bypass nozzle exit ($r_{in-Exit}^{BP}$, Fig. 4b).

The design space of non-axisymmetric exhausts is then characterised with six degrees of freedom (DOF) (Fig. 3 and 4). These encompass the two design variables that control the shear perturbation (ψ_A, θ_A), the mean after-body length ($L_{AFTB}^{BP}/L_{AFTB_{ref}}^{BP}$, Fig. 3), and the three parameters for the perturbation of the bypass trailing edge radius (ψ_R, R/R_{ref}, $\Delta\psi_R$, Fig. 4). Both perturbations can be applied at any arbitrary location in the bypass annulus, where the azimuthal positions (ψ_A, ψ_R) are bounded to cover all the azimuthal extend of the bypass nozzle ($0^o < \psi_{A,R} < 360^o$).

2.3. Computational assessment

Installed powerplant configurations (Fig. 1c) were assessed with inviscid and viscous CFD methods [39]. The inviscid method was based on the numerical resolution of the compressible Euler equations and was used to sample the design space and generate exhaust databases. The viscous method was based on the resolution of the Favre-Averaged Naiver Stokes equations and was used to assess the optimum designs. For the viscous method, the steady-state solver was implicit, density-based and was coupled with second order convective schemes and the $k-\omega$ SST turbulence model [40]. The dynamic viscosity of the fluid was calculated with the Sutherland's law [41] in both methodologies.

The boundary conditions were related to the mid-cruise operation of the CRM (Fig. 5a, Table 1). Pressure inflow conditions were applied on the bypass and core nozzle inlets. These were defined from the target nozzle pressure ratios ($FNPR \approx 2.2$, $CNPR \approx 1.5$, Table 1) and total temperatures. The fan face was modelled as a pressure outlet with a target mass flow that enforced a mass flow capture ratio of $MFCR \approx 0.7$. The computational domain was hemispherical with a diameter of 100 times the CRM reference chord length centred on the CRM nose. This was in accordance with the guidelines proposed by the 4^{th} AIAA drag prediction workshop [35]. A pressure far-field was applied on the hemispherical bounds with a $M_\infty = 0.85$ and static quantities at the cruise altitude ($h = 10668m$, Table 1), coupled with a symmetry condition across the CRM vertical plane. The walls were non-slip for viscous calculations while the Euler CFD method was configured with inviscid slip walls.

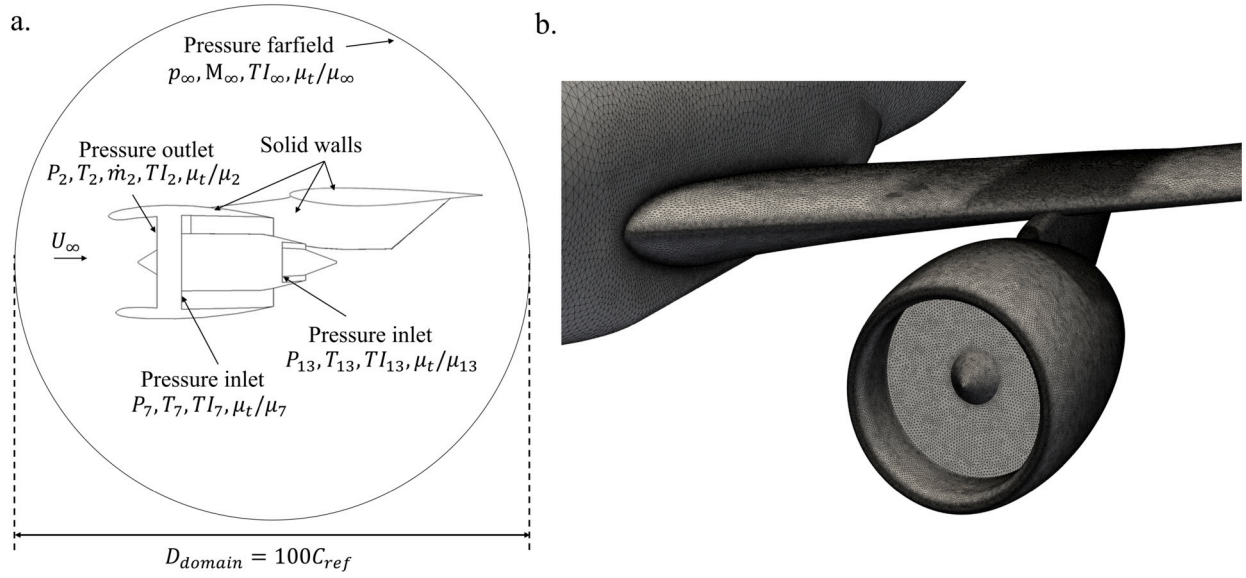


Fig. 5. (a) Schematic of the computational domain and boundary conditions and (b) surface mesh.

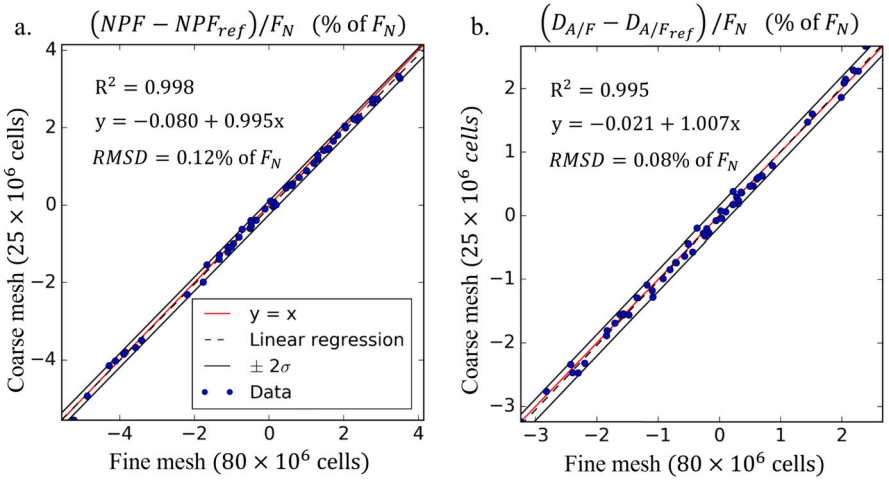


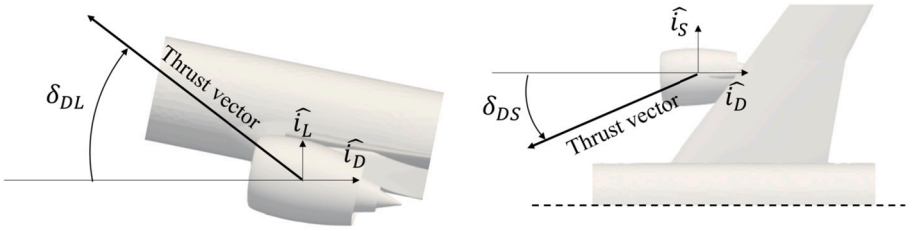
Fig. 6. Effect of mesh density on the Euler CFD method across the design space. The results include (a) ΔNPF and (b) $\Delta D_{A/F}$.

For viscous CFD solutions, the computational grids were unstructured with prismatic layers close to the solid bodies for boundary layer resolution and tetrahedra elsewhere (Fig. 5b). The grids ensured a $y^+ < 1$ throughout the geometry. A grid independence study was carried out where meshes with 220×10^6, 115×10^6 and 60×10^6 cells were assessed. Meshes of approximately 115×10^6 cells were considered sufficient to evaluate installed configurations as these had a grid convergence index (GCI) [42] in Net Propulsive Force (NPF) and airframe drag ($D_{A/F}$) of $GCI_{NPF} = 0.34\%$ and $GCI_{D_{A/F}} = 1.57\%$, respectively. In addition to the verification of the computational meshes, the turbulent CFD methodology was validated with experimental data [6]. The prediction of nozzle flows was validated against the experimental results of the isolated Dual Separate Flow Reference Nozzle (DSFRN) [43]. A Root Mean Squared Deviation (RMSD) between CFD and measurements of 0.033% was obtained for the velocity coefficient across the FNPR range $(1.4 - 2.8)$ with an 80×10^6 cell mesh. The numerical methodology was also validated for the prediction of the installation drag with the CRM experimental data [35]. At design conditions ($C_L = 0.5$), the installation drag was captured within two drag counts of the experimental results [35].

A similar meshing strategy was applied to the Euler CFD method, but with coarser settings. The selection of the Euler CFD mesh was based on the trade-off between accuracy and computational performance. First, a grid independence study was undertaken. For a grid of 80×10^6 cells (fine) the grid convergence indexes were of $GCI_{NPF} = 0.2\%$ and $GCI_{D_{A/F}} = 2.8\%$. For the same mesh, the computations were approximately nine times faster relative to the viscous methodology. However, this was considered insufficient to carry out the design exploration of non-axisymmetric exhausts. For this reason, another mesh of 25×10^6 cells (coarse) was assessed. Fine and coarse grids were employed to assess 96 different non-axisymmetric exhaust designs. It was found that the coarse mesh could predict the variability of the performance metrics in the design space with a root mean squared deviation in NPF and $D_{A/F}$ of $RMSD_{NPF} = 0.0012F_N$ and $RMSD_{D_{A/F}} = 0.0008F_N$ relative to the fine mesh, respectively Fig. 6. With the coarse mesh, the computational time required to assess one design was reduced by a factor of approximately thirty-six relative to the turbulent method. This enabled the gathering of sufficient data to construct response surface models.

2.4. Thrust and drag bookkeeping

A modified near-field method for thrust and drag bookkeeping [44] was used to determine the metrics of interest. The methodology is de-



a. Vertical angles b. Lateral angles

Fig. 7. Definition of the (a) vertical and (b) lateral thrust angles.

tailed in the work of Goulos et al. [6]. A 3D vectorial formulation in the aerodynamic reference frame ($\hat{i}_D, \hat{i}_S, \hat{i}_L$) is considered where all the forces are composed by drag (D), lift (L) and side (S) terms. The overall performance of the complete aircraft system is reported in terms of net vehicle force (NVF). The NVF is directly correlated with cruise fuel burn where $0.01F_N$ increase is approximately 1% reduction in fuel consumption. It is defined as the balance between propulsive and aerodynamic forces (Eq. (2)) in the drag direction ($\hat{i}_D$) and is composed by the modified gross propulsive force ($(GPF^*)_D$), intake momentum (F_{G0}) and the aircraft drag ($D_{A/C}$).

$$NVF = (GPF^*)_D - F_{G0} - D_{A/C} \tag{2}$$

The GPF^* is computed with gauge stream forces at nozzle inlets and pressure and viscous forces on the walls within the exhaust post-exit stream tube. In addition, GPF^* is corrected to account for the cycle mass flow and avoid discrepancies between intake and nozzles. The aircraft drag ($D_{A/C}$) combines the modified nacelle (D^*_{nac}) and airframe ($D_{A/F}$) drag terms (Eq. (3)). The modified nacelle drag accounts for the pre-entry and wall forces over the fan cowl and drag domain of the pylon while the $D_{A/F}$ includes the forces on the wing, fuselage and tail of the CRM.

$$D_{A/C} = D^*_{nac} + D_{A/F} \tag{3}$$

The resultant lift component of propulsive and aerodynamic forces is the aircraft lift ($L_{A/C}$) (Eq. (4)). The aircraft lift coefficient ($C_{L_{A/C}}$, Eq. (5)) is normalised with the free-stream dynamic pressure (q_∞) and the CRM wing reference area (A_{ref}) [45]. The wing reference area is defined with the Wimpress method and has a value of $A_{ref} = 191.85$ m^2 for half CRM model [45]. In this method, the wing is extruded at the root until the fuselage centreline is met. The reference area is the projection of the extruded wing on the $\hat{i}^{A/F}_x - \hat{i}^{A/F}_y$ plane. All the metrics are then expressed for the CRM mid-cruise conditions with $C_{L_{A/C}} = 0.5$.

$$L_{A/C} = (GPF^*)_L + L^*_{nac} + L_{A/F} \tag{4}$$

$$C_{L_{A/C}} = \frac{L_{A/C}}{q_\infty A_{ref}} \tag{5}$$

In addition to force metrics, nozzle discharge coefficients are also required. Discharge coefficients (Eq. (6)) at the bypass (C_d^{BP}) and core (C_d^{CR}) nozzles are defined as the normalisation of the CFD-computed mass flows ($\dot{m}_{CFD}$) with their ideal mass flow per unit area ($\left(\frac{\dot{m}}{A}\right)_{id}$) and throat area ($A_{th}$).

$$C_d = \frac{\dot{m}_{CFD}}{\left(\frac{\dot{m}}{A}\right)_{id} A_{th}} \tag{6}$$

For the design of non-axisymmetric exhausts (sub-index 2, e.g. $()_2$), it is more convenient to express the metrics as changes relative to the baseline axisymmetric configuration (sub-index 1, e.g. $()_1$). The changes in the force terms are normalised with the standard nominal thrust (F_N, Eq. (7)) and are defined such that a positive value implies a benefit in the aircraft performance. Moreover, the intake momentum remains constant relative to the baseline configuration. For this reason, the increase in NVF (ΔNVF) is expressed as the sum of the changes in modified gross propulsive force and aircraft drag (Eq. (8))

$$\Delta F = \frac{F_2 - F_1}{F_N} \tag{7}$$

$$\Delta NVF = (\Delta GPF^*)_D + \Delta D_{A/C} \tag{8}$$

2.4.1. Thrust vector angles

Modifications of the bypass nozzle trailing edge are likely to affect the already strong 3D features of the flow. These modifications may change the magnitude and orientation of the propulsive force vector. Thrust angles (δ_{DL} and δ_{DS}) are defined in aerodynamic coordinates as the angles of the modified gross propulsive force vector (Eq. (9) and (10)). The vertical thrust vector angle (δ_{DL}, Eq. (9)) is the angle between the lift ($\hat{i}_L$) and drag ($\hat{i}_D$) components of the gross propulsive force (Fig. 7a) while the lateral thrust vector angle (δ_{DS}, Eq. (10)) is defined between the lateral ($\hat{i}_S$) and drag ($\hat{i}_D$) components of the same metric (Fig. 7b).

$$\delta_{DL} = atan\left(\frac{(GPF^*)_L}{(GPF^*)_D}\right) \tag{9}$$

$$\delta_{DS} = atan\left(\frac{(GPF^*)_S}{(GPF^*)_D}\right) \tag{10}$$

2.4.2. Decomposition of the propulsive force

To quantify the thrust vectoring, the propulsive force ($(\Delta GPF^*)_D$) is decomposed into magnitude effects ($(\Delta GPF^*_{mag})_D$) and thrust vectoring terms ($(\Delta GPF^*_{vec})_D$) (Eq. (11)). $(\Delta GPF^*_{mag})_D$ is defined from the change in the modulus of GPF^* (Eq. (12)) while the thrust vectoring accounts for the force component redistribution due to changes in thrust angles (Eq. (13)) (Fig. 8a).

$$(\Delta GPF^*)_D = (\Delta GPF^*_{mag})_D + (\Delta GPF^*_{vec})_D \tag{11}$$

$$(\Delta GPF^*_{mag})_D = \left(GPF^*_2 - |GPF^*_1|\frac{GPF^*_2}{|GPF^*_2|}\right)_D \tag{12}$$

$$(\Delta GPF^*_{vec})_D = \left(|GPF^*_1|\frac{GPF^*_2}{|GPF^*_2|} - GPF^*_1\right)_D \tag{13}$$

The thrust vectoring term is further split into the vertical ($\Delta GPF^*_{\delta_{DL}}$) and lateral ($\Delta GPF^*_{\delta_{DS}}$) contributions that arise from changes in δ_{DL} and δ_{DS}, respectively (Eq. (14)). Each term is estimated assuming the isolated effect of the target angle ($\Delta GPF^*_{\delta_{iso-DL}}$, $\Delta GPF^*_{\delta_{iso-DS}}$) (Eq. (15), Fig. 8b,c). Weighting coefficients for each effect (W_{DL} and W_{DS}) are computed as the ratio of an individual effect relative to the sum of both isolated contributions ($\Delta GPF^*_{\delta_{iso-DL}} + \Delta GPF^*_{\delta_{iso-DS}}$, Eq. (16)). These coefficients are applied to $(\Delta GPF^*_{vec})_D$ and the final metric is obtained ($\Delta GPF^*_{\delta_{DL}}$, $\Delta GPF^*_{\delta_{DS}}$, Eq. (17)). In equations (15)-(17), the process is described only for the vertical vectoring (δ_{DL}). However, it is exactly the same for the lateral effect (δ_{DS}).

$$(\Delta GPF^*_{vec})_D = \Delta GPF^*_{\delta_{DL}} + \Delta GPF^*_{\delta_{DS}} \tag{14}$$

$$\Delta GPF^*_{\delta_{iso-DL}} = |GPF^*_{ref}|(\cos\delta_{DS_2} - \cos\delta_{DS_1}) \tag{15}$$

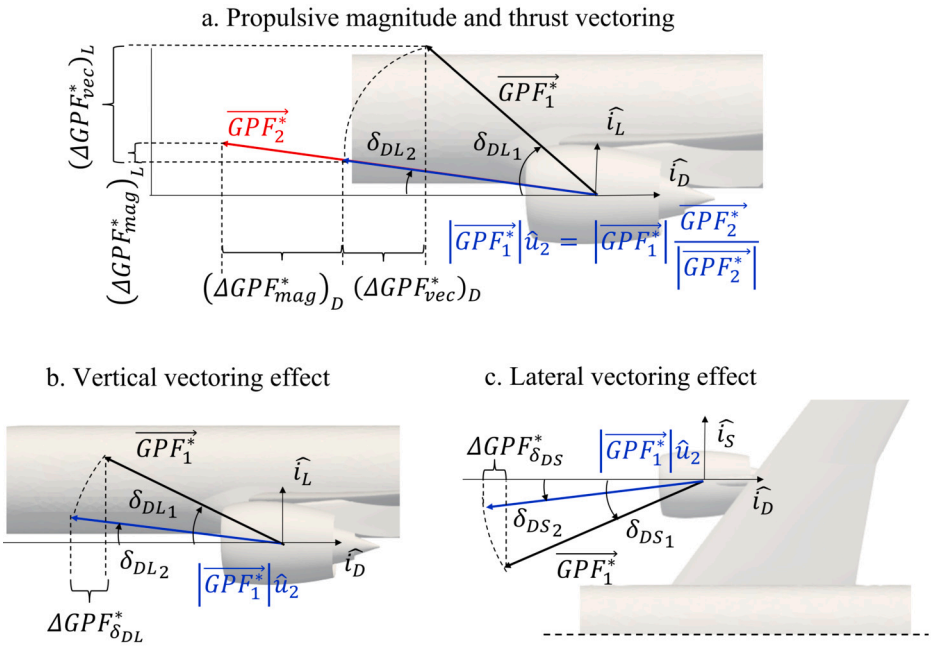


Fig. 8. Decomposition of the propulsive force. (a) Propulsive magnitude and thrust vectoring split, (b) vertical vectoring and (c) lateral vectoring effects.

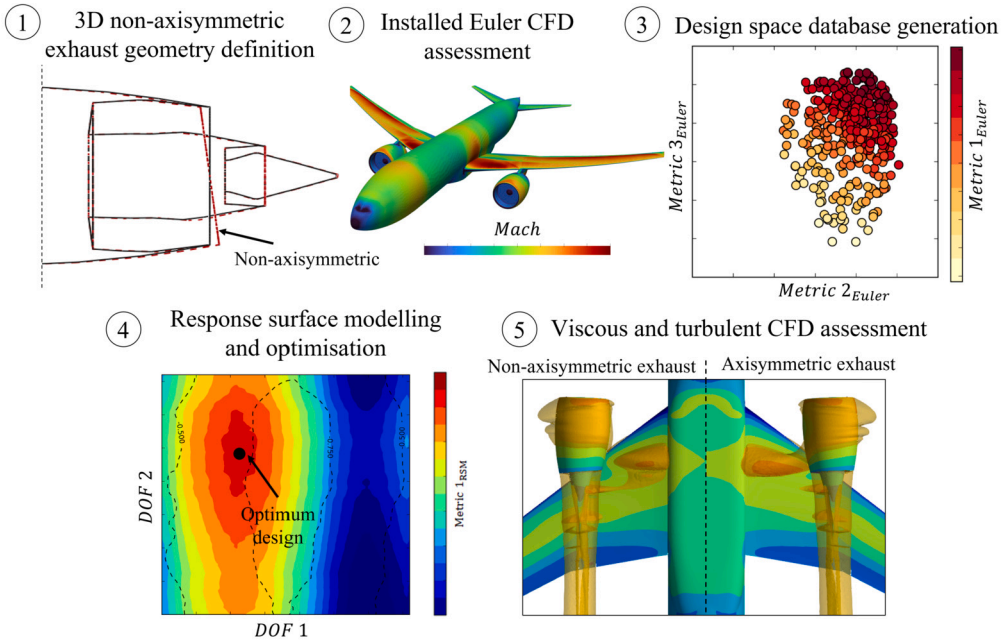


Fig. 9. Schematic of the design space exploration and optimisation methodology.

$$W_{DL} = \frac{\Delta GPF^*_{\delta_{iso-DL}}}{\Delta GPF^*_{\delta_{iso-DL}} + \Delta GPF^*_{\delta_{iso-DS}}} \tag{16}$$

$$\Delta GPF^*_{\delta_{DL}} = (\Delta GPF^*_{vec})_D W_{DL} \tag{17}$$

2.5. Design space exploration and optimisation methods

The parametrisation of exhaust geometries, the installation of the propulsion system with the airframe and the CFD assessment of the designs were coupled in a systematic design methodology (Fig. 9). This encompassed the design of experiment (DOE), Response Surface Modelling (RSM) and RSM based optimisation.

2.5.1. Design of experiment

During the design of experiment, the design space was sampled to compile a database of non-axisymmetric exhausts. The method comprised an optimal Latin hypercube sampling (LHS) [46] where a total of 480 exhaust designs were distributed across the design space (Fig. 9, number 3). This is a ratio of samples per design variable of $N_S/N_{DOF} = 80$, similar to previous investigations for installed propulsion system configurations [30].

2.5.2. Response surface modelling

All the designs in the database were assessed with Euler CFD and the aerodynamic metrics of interest were calculated. With the resultant data, Response Surface Models (RSMs) were formulated (Fig. 9, number 4). The Gaussian regression process (Kriging) [17,47] modelled

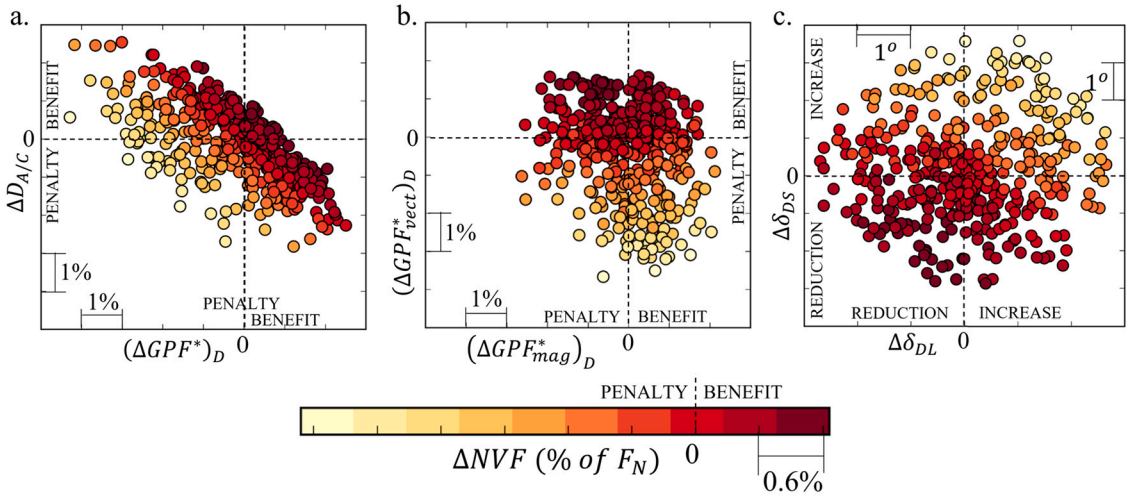


Fig. 10. Summary of the design space exploration results with splits of (a) $(\Delta GPF^*)_D$ and $\Delta D_{A/C}$, (b) $(\Delta GPF^*_{vec})_D$ and $(\Delta GPF^*_{eff})_D$, (c) $\Delta\delta_{DL}$ and $\Delta\delta_{DS}$.

the response of the non-axisymmetric exhaust design space. Detailed mathematical formulations of the Gaussian regression process can be found in the literature [18]. The hyper-parameters of the Kriging RSM were tuned for the best response of the model using a leave-one-out (LOO) cross validation methodology [48]. The RSM predictions for a set 480 non-axisymmetric exhaust designs were correlated with the original CFD results in terms of linear regression and root mean squared deviation (RMSD). The best response of the model was with quadratic regression and absolute exponential correlation functions, together with a nugget size of $\epsilon = 1 \times 10^{-7}$. The verification results for ΔNVF, $\Delta(GPF^*_{mag})_D$ and $\Delta(GPF^*_{\delta_{DS}})_D$ indicated a coefficient of determination (R^2) of $R^2 = 0.96$, 0.984 and 0.963, a linear slope of $m = 0.945$, 0.975 and 0.963 and a root mean squared deviation of $RMSD = 0.002F_N$, $0.0012F_N$ and $0.0018F_N$, respectively.

2.5.3. Design optimisation

Response surface models drove the optimisation process in which a Genetic Algorithm (GA) [49] was selected as in other nacelle [23,24] and exhaust [26,27] optimisation studies. The optimisation parameters were conservative to ensure the convergence of the process. In addition, the optimisation was bounded by the discharge coefficients. From a design point of view, variations of discharge coefficients can be absorbed by small variations of the nozzle areas. Within this work, it was found that differences up to $|\Delta C_d^{BP}| \leq 1\%$ of $C_{d_{ref}}^{BP}$ and $|\Delta C_d^{CR}| \leq 6\%$ of $C_{d_{ref}}^{CR}$ could be accommodated by small changes in the nozzle exit areas without compromising the NVF. Once the optimisation algorithm identified an optimum non-axisymmetric exhaust design, this was assessed with the viscous and turbulent CFD method (Fig. 9, number 5).

3. Results and discussion

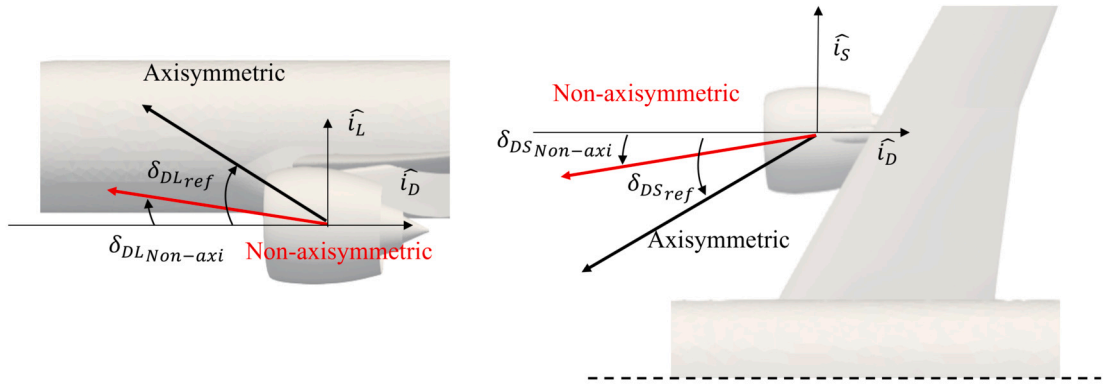
Non-axisymmetric exhausts were designed for a close coupled installation position. First, the design space was analysed with the results of the design of experiment to identify the general trends. After that, several candidate designs were identified with the RSM based optimisation. These encompassed designs optimised for different performance requirements which were compared in terms of performance and aerodynamics. Finally, a set of design recommendations for non-axisymmetric exhaust systems were derived from the sensitivities of the optimum design to the different degrees of freedom.

3.1. Analysis of the design space

The exploration of the design space with the inviscid CFD method indicates a great variability of ΔNVF (Fig. 10a). The levels of performance range from a penalty of $\Delta NVF = -0.036F_N$ up to a benefit of $\Delta NVF^{MAX} = 0.013F_N$ relative to the baseline axisymmetric exhaust. Within this range, a third of all designs have a benefit in performance compared with the baseline, 17.3% of the population with $\Delta NVF > 0.004F_N$ and 5.2% of $\Delta NVF > 0.008F_N$. These indicate that it may be possible to improve the overall aircraft performance with non-axisymmetric exhausts. The NVF is governed by the balance of propulsive ($(\Delta GPF^*)_D$) and drag ($\Delta D_{A/C}$) forces (Fig. 10a). The former varies between $-0.04F_N < (\Delta GPF^*)_D < 0.027F_N$ while the later ranges between $-0.025F_N < \Delta D_{A/C} < 0.025F_N$. The majority of the best designs ($\Delta NVF > 0.008F_N$) lie in the region of beneficial propulsive force. However, not all of the best designs reduce the aircraft drag. The split of $(\Delta GPF^*)_D$ into vectoring ($(\Delta GPF^*_{vec})_D$) and magnitude ($(\Delta GPF^*_{mag})_D$) contributions (Fig. 10b) highlights the increased importance of thrust vectoring. Most of the designs with $\Delta NVF > 0.008F_N$ benefit the thrust vectoring ($(\Delta GPF^*_{vec})_D > 0.01F_N$) while the magnitude of GPF^* is penalised. This trade-off effect indicates that for installed configurations it is more effective to modify the thrust vector angles and align the thrust vector with the drag axis ($\hat{i}_D$) (Fig. 11) than to increase the magnitude of the propulsive force. The thrust vectoring benefit in ΔGPF^* arises from a reduction of thrust vector angles (δ_{DL}, δ_{DS}) by up to 3^o relative to the reference configuration and it is dominated by the lateral component (δ_{DS}, Fig. 10c). This result indicates that non-axisymmetric exhausts are effective to control the thrust vectoring. In terms of discharge coefficients, ΔC_d^{BP} has a variation of 1.2% across the design space while ΔC_d^{CR} changes between $-17\% < \Delta C_d^{CR} < 5\%$, relative to the reference. The designs with $\Delta NVF > 0F_N$ are spread across the different values of the discharge coefficients. This result emphasises the importance of limiting the metrics in the optimisation.

To identify the regions of the design space that benefit the NVF, the dataset is presented in the form of banded histograms with intervals of one third of the maximum ΔNVF in the DSE (Fig. 12). The histograms display the density distribution of designs at each band of benefit. Fig. 12 indicates that the shear perturbation (ψ_A, θ_A) governs ΔNVF. Designs with higher net vehicle force ($\Delta NVF/\Delta NVF^{MAX} > 0.66$) are configured with inboard-sheared bypass exhausts ($0^o < \psi_A < 180^o$) and notable shear angles (θ_A). The optimum placement of the perturbation of the bypass trailing edge radius (ψ_R) also plays a role whereby the most beneficial location is at the inboard-side. Most of the designs with $\Delta NVF/\Delta NVF^{MAX} > 0.33$ have a value of ψ_R between 180^o and 300^o.

Although the characterisation and analysis of the design space is addressed with the low-fidelity CFD method, it provides a good overview of the trade-offs between performance metrics once the effects of the propulsion system integration are considered. The potential benefit of non-axisymmetric exhausts is proven to arise mostly from a better align-



a. Reduction of vertical thrust vector angle b. Reduction of lateral thrust vector angle

Fig. 11. Reduction of (a) vertical and (b) lateral thrust vector angles produced by non-axisymmetric exhausts.

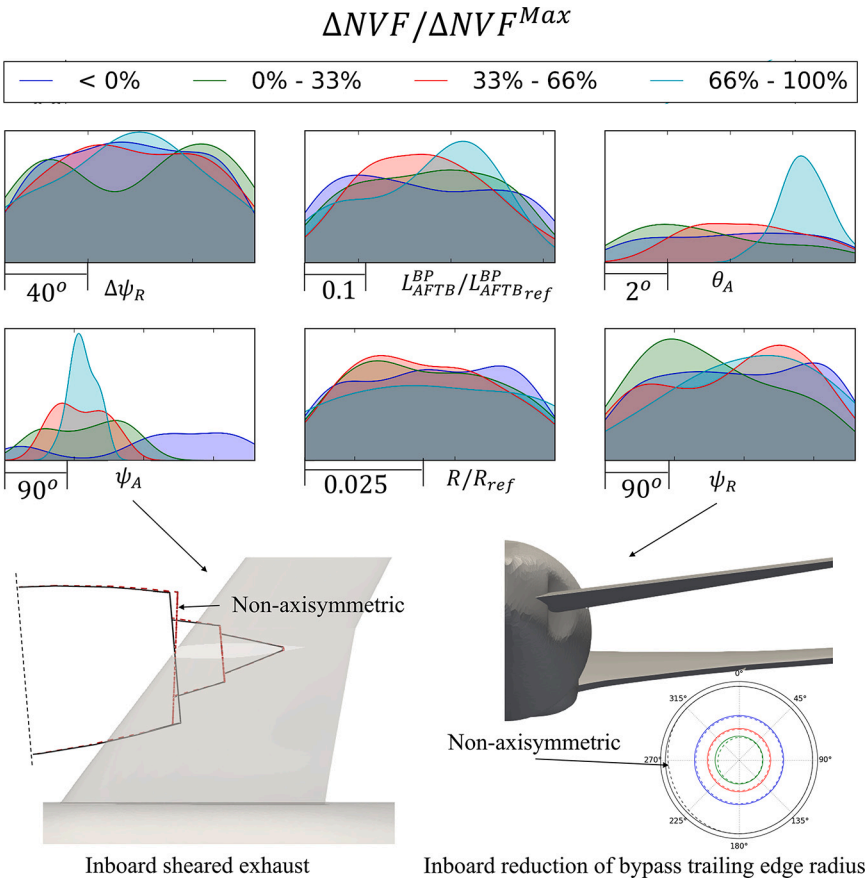


Fig. 12. Histograms of the distribution of designs in the design space. The database is classified in bands of different levels of ΔNVF.

ment of the thrust vector with the drag direction, dominated by the lateral vectoring term.

3.2. Optimisation of installed non-axisymmetric exhaust systems

The low-fidelity dataset is utilised to formulate RSMs that guide the optimisation process. Four optimisations identified candidate designs for different performance requirements (D1, D2, D3 and D4, Table 2). Design D1 is the result of the maximisation of ΔNVF. The purpose of this optimisation is to find the best design in terms of aircraft performance that can be obtained with a low-fidelity data driven optimisation. Design D2 is obtained from the maximisation of $(\Delta GPF^*_{mag})_D$. The objective of D2 is to understand if ΔNVF can benefit from an exhaust focused design. The optimisation of this metric is equivalent to the maximisation of $|C^*_v|$. Design D3 is selected from the maximisation of $\Delta GPF^*_{\delta_{DS}}$. The goal is to quantify the benefits in NVF that result from the optimisation of the lateral thrust-vectoring and therefore from reductions of the lateral thrust angle (δ_{DS}). Finally, design D4 results from the maximisation of ΔNVF subject to $\delta_{DL} - \delta_{DL_{ref}} > 0^o$ and $(\Delta GPF^*_{mag})_D > 0F_N$. The purpose of D4 is to determine how the effect of constraints in vertical thrust-vectoring and exhaust performance can limit the ΔNVF. The constraint on δ_{DL} prevents the deflection of the exhaust jet towards the wing trailing edge. The second constraint enforces $|C^*_v|$ to be beneficial. Moreover, discharge coefficients are bounded to $|\Delta C_d^{BP}| \leq 1\%$ and $|\Delta C_d^{CR}| \leq 6\%$ in all four optimisations.

The optimum non-axisymmetric exhaust design for maximum ΔNVF (D1) improves the overall aircraft performance by $\Delta NVF =$

Table 2
Summary of the designs identified with the different optimisations. Although not shown in the table, all optimisations are subject to $|\Delta C_d^{BP}| \leq 1\%$ and $|\Delta C_d^{CR}| \leq 6\%$.

Design	Target	Constraint 1	Constraint 2
D1	ΔNVF^{MAX}	-	-
D2	$(\Delta GPF^*_{mag})_D^{MAX}$	-	-
D3	$\Delta GPF^{*MAX}_{\delta_{DS}}$	-	-
D4	ΔNVF^{MAX}	$\Delta\delta_{DL} > 0^o$	$(\Delta GPF^*_{mag})_D > 0\%$

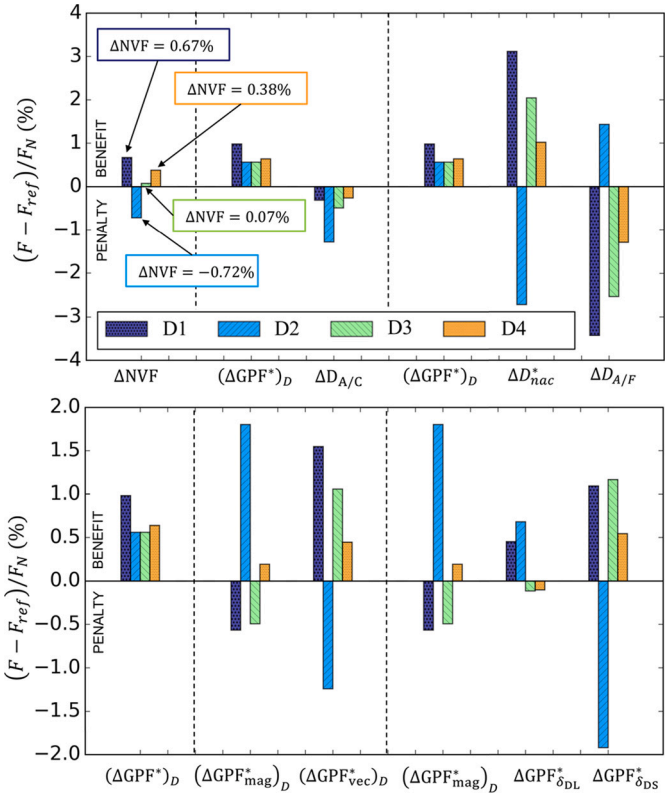


Fig. 13. Thrust and drag accounting decomposition for the four candidate designs. These results are based on viscous and turbulent CFD assessments.

$0.0067F_N$ when assessed with viscous and turbulent CFD (Fig. 13a), relative to the baseline axisymmetric exhaust. This approximately equivalent to a reduction of 0.7% in cruise fuel burn. Therefore, non-axisymmetric exhaust systems can improve the aircraft performance substantially. D4 also improves the net vehicle force ($\Delta NVF = 0.0038F_N$) (Fig. 13a). However, the benefit is reduced by approximately 40% relative to D1 due to the extra constraints on vertical thrust vectoring ($\Delta\delta_{DL} > 0^o$) and propulsive force magnitude ($(\Delta GPF^*_{mag})_D > 0F_N$). On the other hand, the maximisation of the overall exhaust performance (design D2) and lateral vectoring (design D3) is not effective to improve NVF (Fig. 13). D2 penalises NVF by $-0.0072F_N$ while D3 improves it by $\Delta NVF = 0.0007F_N$, compared to the baseline.

For D1, the improvement in NVF ($\Delta NVF = 0.0067F_N$) arises from a benefit in propulsive force ($(\Delta GPF^*)_D = 0.0098F_N$) which is offset by a penalty in aircraft drag ($\Delta D_{A/C} = -0.0031F_N$). To understand the drivers of the performance, the split of propulsive and drag metrics is evaluated further (Fig. 13). The penalty in aircraft drag is the result of a balance between a beneficial effect on the nacelle drag ($\Delta D^*_{nac} = 0.031F_N$) and a penalising effect on the airframe component ($\Delta D_{A/F} = -0.034F_N$). The improvement in gross propulsive force is governed by thrust vectoring. The metric is benefited by $(\Delta GPF^*_{vec})_D = 0.0155F_N$ and is dominated by the lateral component of the effect ($\Delta GPF^*_{\delta_{DS}} = 0.011F_N$ and $\Delta GPF_{\delta_{DL}} = 0.0045F_N$). This results from reductions in thrust vector angles of $\Delta\delta_{DL} = -0.8^o$ and $\Delta\delta_{DS} = -2.3^o$ relative to the baseline (Table 3). For the baseline axisymmetric exhaust, the lateral thrust angle (δ_{DS}) is approximately 2.7^o greater than ϕ_{toe} (Table 3). This indicates that the effects of the propulsion system installation deflect the thrust vector laterally and reduce the gross propulsive force in the drag direction. Non-axisymmetric configurations of the exhaust (D1, D3 and D4) are effective to counteract the effect and align the thrust vector with the drag axis ($\hat{i}_D$). Opposite to thrust vectoring, the magnitude of GPF^* is penalised by $(\Delta GPF^*_{mag})_D = -0.0057F_N$. Therefore, to improve NVF, the overall performance of the exhaust system is reduced relative to the baseline but the thrust vector is more aligned with $\hat{i}_D$. These results confirm the strong coupling between thrust and drag forces and the need for an optimisation methodology that considers the effects of the propulsion system installation.

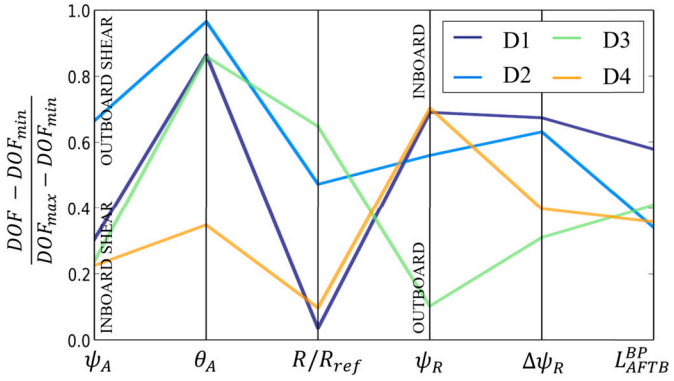


Fig. 14. Parallel coordinates chart of the optimum designs.

Table 3
Vertical (δ_{DL}) and lateral (δ_{DS}) thrust vector angles of the baseline configuration and optimum non-axisymmetric exhaust designs. The table also includes the pitch (ϕ_{pitch}) and toe (ϕ_{toe}) angles.

Design	$\delta_{DL}(^o)$	$\delta_{DS}(^o)$	$\phi_{pitch}(^o)$	$\phi_{toe}(^o)$
Baseline	5.02	4.96	1.75	2.25
D1	4.23	2.66	1.75	2.25
D2	3.79	7.44	1.75	2.25
D3	5.20	2.41	1.75	2.25
D4	5.18	3.98	1.75	2.25

In terms of the non-axisymmetric perturbations of the bypass trailing edge (Fig. 14), D1 (ΔNVF^{MAX}) follows the trends identified during the analysis of the design space. D1 is configured with an inboard-sheared fan cowl and a reduced bypass trailing edge radius at the inboard-side. To evaluate the different mechanisms by which non-axisymmetric configurations alter the exhaust, nacelle and airframe performance, the different designs are compared. While D1 has an inboard-sheared bypass nozzle, D2 is sheared towards the outboard-side (Fig. 14). To improve $(\Delta GPF^*_{mag})_D$, the exhaust is sheared towards the opposite side relative to D1. However, this misaligns the thrust vector further relative to the baseline as the lateral thrust vector angle is increased from $\delta_{DS} = 4.96^o$ (baseline) to 7.44^o (D2) (Table 3). The penalising effect in lateral thrust vectoring ($\Delta GPF^*_{\delta_{DS}} = -0.0192F_N$) offsets the gain in magnitude ($(\Delta GPF^*_{mag})_D = 0.018F_N$). The maximisation of the lateral thrust vectoring (design D3) results in a similar shear configuration as D1 but at a reduced azimuthal position (Fig. 14). This demonstrates the impact of ψ_A on thrust vectoring. Although D3 reduces the lateral vector angle from $\delta_{DS} = 4.96^o$ (baseline) to 2.41^o (D3) (Table 3), the vertical angle increases and limits the benefit in GPF^*. Finally, D4 is similar

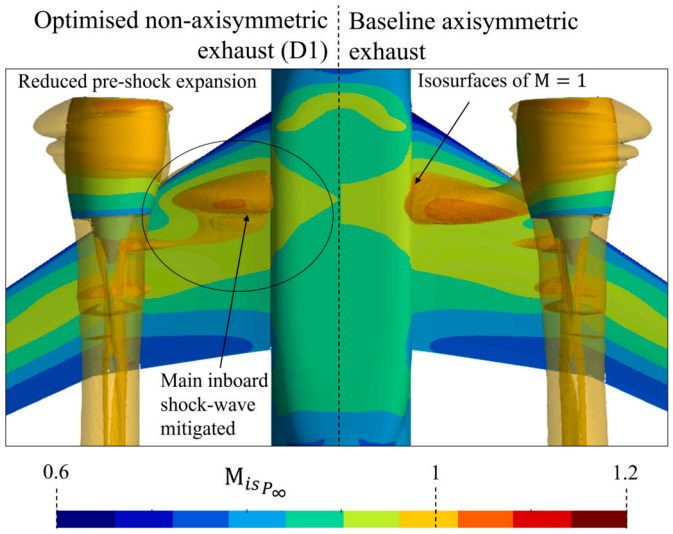


Fig. 15. Comparison of the aerodynamics of an optimised non-axisymmetric exhaust (D1, left) with the baseline axisymmetric configuration (right). The figure includes isentropic Mach number distributions based on P_∞ and M= 1 isosurfaces over the pressure side of the wing.

to D1 (Fig. 14). However, the constraints in $\Delta\delta_{DL}$ and in $(\Delta GPF^*_{mag})_D$ (Table 2) lead to a reduced shear angle (θ_A) and lower ψ_A relative to D1. Nevertheless, the perturbation in the bypass trailing edge radius remains similar in both designs (Fig. 14). This indicates that the radius perturbation can benefit the NVF without changing substantially the magnitude and direction of GPF^*.

In conclusion, exhausts designed for maximum ΔNVF are configured with inboard-shear and reduced bypass trailing edge radius at the inboard side. This aligns the thrust vector with the drag axis and reduces the modified nacelle drag, which benefits the NVF. Moreover, the optimisation of performance metrics related to the exhaust ($\Delta GPF^*_{\delta_{DS}}$, $(\Delta GPF^*_{mag})_D$) does not improve ΔNVF.

3.3. Aerodynamic mechanisms

Non-axisymmetric exhausts modify the aircraft performance at a system level. From an aerodynamics point of view, it is the result of a combination of two different mechanisms that impact the propulsion system and the airframe. First, non-axisymmetric exhausts alter the inboard shock field that results from the propulsion system installation. Second, the asymmetric geometry of the bypass exit plane and after-body modify the expansion of the bypass flow azimuthally.

3.3.1. Mitigation of the inboard shock-field

While design D1 exhibits the highest NVF ($\Delta NVF = 0.0067F_N$), it also penalises the aircraft drag ($\Delta D_{A/C} = -0.0031F_N$). The increase in aircraft drag arises from the shock-waves and pre-shock expansions at the inboard side of the propulsion system (Fig. 15). Designs that reduce the fan cowl length at the inboard side (D1, D3, D4) mitigate the first shock and therefore reduce the strength of the pre-shock expansion (Fig. 15). This has opposite effects on the nacelle and airframe (Fig. 16). It increases the static pressure at the aft of the nacelle relative to the baseline, which benefits the nacelle drag by $\Delta D^*_{nac} = 0.031F_N$. However, the same static pressure increase is detrimental for the airframe ($\Delta D_{A/F} = -0.034F_N$). Given the design of the CRM wing pressure-side, lower static pressures at the inboard of the propulsion systems reduce the airframe drag. However, this arises from a reduction in the CRM lift that is counteracted by the vertical component of the propulsive force to ensure a trimmed $C_{L_{A/C}} = 0.5$.

Exhausts that are sheared towards the inboard side reduce the adverse aerodynamic interference of the installation. Inboard-sheared configurations have an increased flow area between fan cowl and wing (Fig. 17a). The bypass trailing edge is displaced forward at the inboard-side, which offsets the nacelle from the wing locally. This increases the effective flow area in the region and prevents the flow from reaching sonic conditions near the fan cowl. Fig. 17b illustrates the effect. For the baseline configuration, the sonic region extends between wing, fuselage and nacelle. However, for design D1, the increased gully area reduces the magnitude of the sonic region. The opposite is observed for D2 (Fig. 16c). D2 is configured with an bypass exhausts that is sheared towards the outboard side. This increases the overlap between fan cowl and wing at the inboard side. This configuration strengthens the pre-shock expansion and shock-wave, which penalises the nacelle ($\Delta D^*_{nac} = -0.0272F_N$) and benefits the airframe ($\Delta D_{A/F} = 0.0144F_N$) drag components, relative to the baseline. In addition to the impact on drag metrics, changes in the inboard-shock field alter the static pressure distributions near the bypass nozzle exit plane. This impacts the discharge coefficients of the bypass and core nozzle through flow suppression mechanisms.

3.3.2. Non-axisymmetric expansion of the bypass flow

Non-axisymmetric configurations of the bypass exhaust modify the expansion of the jet flow azimuthally. Even though the overall bypass area is maintained to the same value as the baseline exhaust, the azimuthal distribution of the bypass area changes. This, combined with the variation of external static pressure that results from the installation interference, modifies the effective nozzle pressure ratio ($NPR_e = P_{inlet}/p_{exit}$) azimuthally. The bypass exhaust system is no longer choked around the whole 360^o annulus (Fig. 18). Instead, local subsonic and under-expanded flow regions appear at opposite azimuthal locations. Inboard-sheared designs (D1, D3, D4) are characterised by a locally under-expanded flow at the outboard side of the propulsion system and a subsonic region at the inboard side, where the fan cowl is shorter (Fig. 18). The subsonic region is partly affected by the pylon through flow blockage and total pressure losses. Moreover, the design of the after-body also impacts the bypass flow expansion downstream of the nozzle exit plane. The after-body design method imposes circular core cowl trailing edges at uniform axial positions. This geometric constraint results in non-uniform distributions of the core cowl boat tail angle (β_{cc}, Fig. 3). For inboard-sheared nozzles, β_{cc} is steeper where the fan cowl is longer, which increases the strength of the flow expansion downstream of the bypass nozzle exit plane.

The aerodynamic interference of the powerplant installation modifies the shape of the exhaust plume as well as the mass (ρv_D), mo-

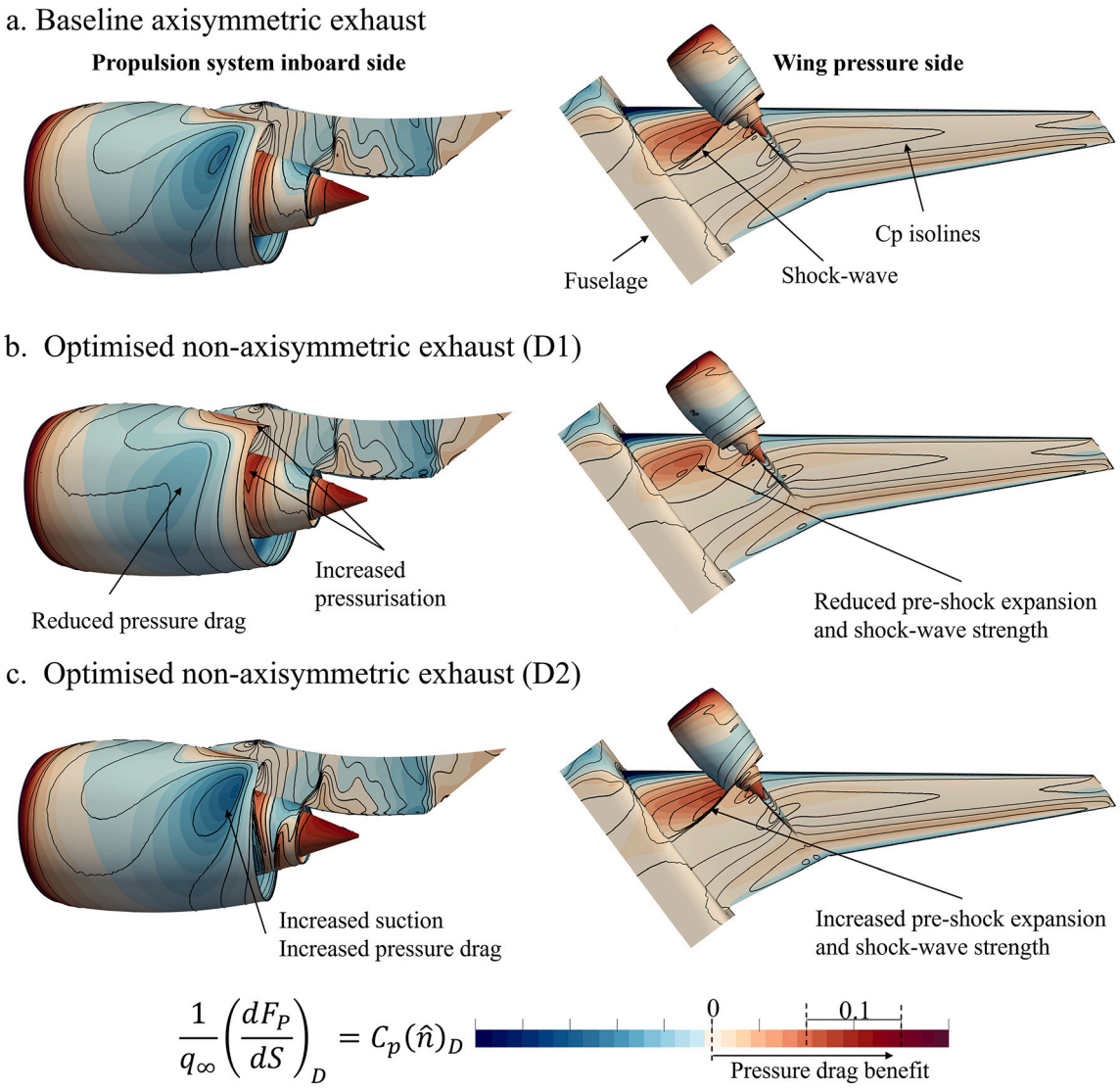
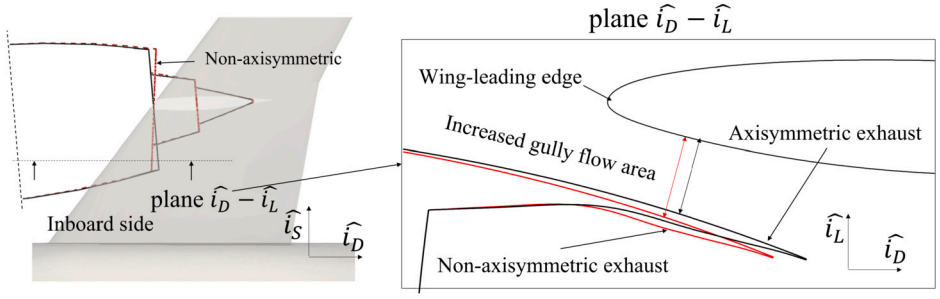


Fig. 16. Pressure drag distributions ($C_p(\hat{n})_D$) over the propulsion system inboard side (left) and wing pressure side (right) of the (a) axisymmetric baseline, (b) design D1 and (c) design D2. Ti figure also includes isolines of pressure coefficient (C_p).

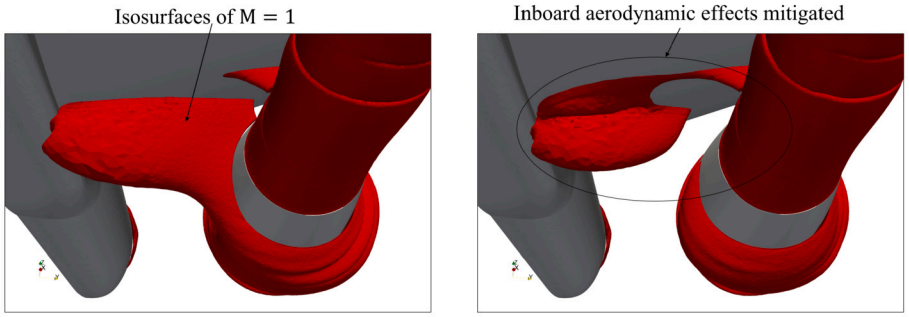
mentum (ρv_D^2) and flow angle distributions inside the jet. These effects increase the asymmetries of the exhaust flow and penalise the gross propulsive force through an increase of the lateral thrust vector angle. Non-axisymmetric configurations of the bypass nozzle can effectively counteract the detrimental effects and reduce the asymmetries within the jet. This is the consequence of a favourable change of plume shape, mass and momentum flux distributions and jet flow angles (Fig. 19). The mechanism can be understood as a recovery of the jet symmetry that results from non-axisymmetric exhaust geometries. The mass flux distributions (ρv_D, Fig. 19a) of designs that are sheared towards the inboard side (D1 and D3) are more left-to-right symmetric relative to the baseline. On the other hand, the asymmetry is accentuated in design D2 as the fan cowl is sheared towards the outboard side. In terms of momentum flux distributions (ρv_D^2, Fig. 19b), D1 has an increased extend of high ρv_D^2 region at the inboard-side, relative to the baseline configuration. For the lateral flow angle ($atan(v_S/v_D)$, Fig. 19c), inboard-shared designs as D1 and D3 direct the flow towards the inboard-side. The lateral flow angle is modified azimuthally and changes the jet deflection. This can be seen for design D3, where negative lateral flow angles (inboard directed flow) are exacerbated at the outboard side.

3.4. Sensitivities of the design space and limitations

The response surface models of the performance of non-axisymmetric exhausts are used to visualise the design space sensitivities and to derive trade-offs and recommendations. Design sensitivity maps (Fig. 20) are obtained varying pairs of degrees of freedom within their respective bounds. For each perturbation, the unperturbed design variables are maintained at the values of the optimum design (D1). Fig. 20 shows the response of the RSM in terms of ΔNVF and thrust vector angles. These include contour lines of ΔC_d^{BP} and ΔC_d^{CR} together with a representation of the regions of the design space where the imposed limits on discharge coefficients are breached (shaded area). The maps were obtained by perturbing the RSM around D1. In addition, the rest of the optimum designs are also represented (dots). The parameters that control the shear perturbation (ψ_A, θ_A) are the dominant design variables to improve NVF (Fig. 20a,b,c). This perturbation directly affects the thrust vector angles and the inboard shock-field and should be configured so the bypass exhaust is sheared towards the inboard side, with a longer nacelle at the outboard side ($\psi_A < 180^o$). Therefore, shear can be used to control thrust vectoring and establish trade-offs between thrust angles and benefits in NVF (Fig. 20d,e). The perturbation of the bypass trailing edge radius has a reduced impact on NVF compared



a. Schematics of the effect of the fan cowl length on the overlap between nacelle and wing



b. Sonic surfaces at the propulsion system inboard side

Fig. 17. Effect of non-axisymmetric exhausts on the inboard aerodynamics. (a) Schematics of the overlap between nacelle and wing and (b) rear views of axisymmetric (left) and non-axisymmetric (right, D1) exhausts. Red isosurfaces are of M= 1.

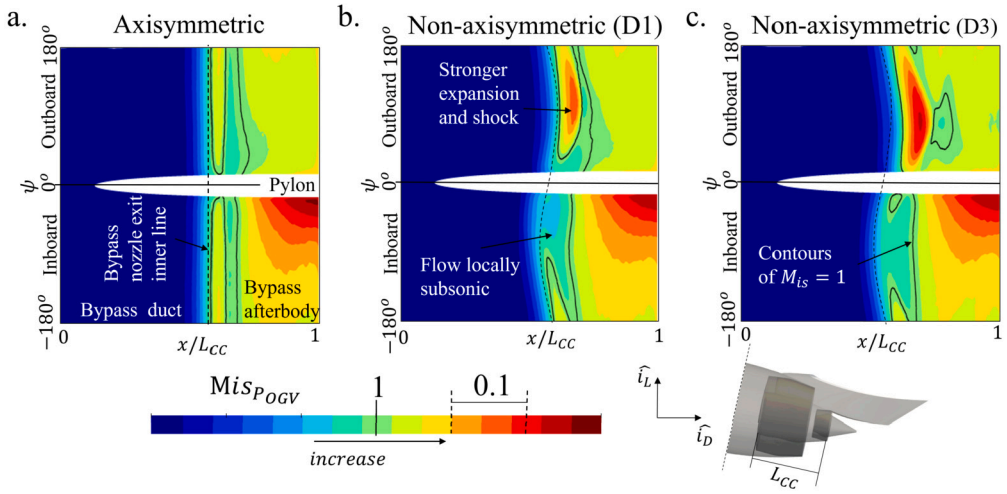


Fig. 18. Isentropic Mach number distributions, based on the OGV total pressure (P_{OGV}), on the unwrapped core cowl surfaces. (a) Baseline axisymmetric exhausts, (b) design D1 (ΔNVF^{Max}) and (c) design D3 ($\Delta GPF^{*,Max}_{\delta_{DS}}$).

with shear (Fig. 20b). The NVF is maximum when the radial bump is placed at the inboard side ($\psi_R > 180^o$). This parametrisation could be configured to improve NVF without altering the thrust vector angles, as these are unaffected by the perturbation. The mean after-body length ($L^{BP}_{AFTB}/L^{BP}_{AFTB_{ref}}$) also influences NVF, but the effect is reduced relative to the perturbations of the bypass trailing edge (Fig. 20c). However, the same design parameter has a notable impact on ΔC_d^{CR} (Fig. 20c).

This work has developed an aerodynamic design method for separate-jet exhausts where there are complex interactions between the propulsion system and the airframe. It highlights an approach for the design space evaluation of installed power-plants which could potentially be adopted for other configurations to include nacelle design, pylon design, installation position, engine specific thrust class as well as different exhaust systems. The method is restricted to the optimisation of exhausts that are parametrised with six degrees of freedom. However, perturbations of the bypass trailing edge modify the geometry of the fan cowl azimuthally. For this reason, an extension of the method for the combined optimisation of exhaust system and fan cowl could lead to further NVF benefits. Another limitation is the use of inviscid calculations to guide the optimisation process. Although the method identifies better designs than the baseline, an optimisation based on viscous simulations could provide further benefits. Although such an optimisation is challenging due to computational cost, multi-fidelity design methods that combine inviscid and viscous CFD could be used to improve the reliability of the design process.

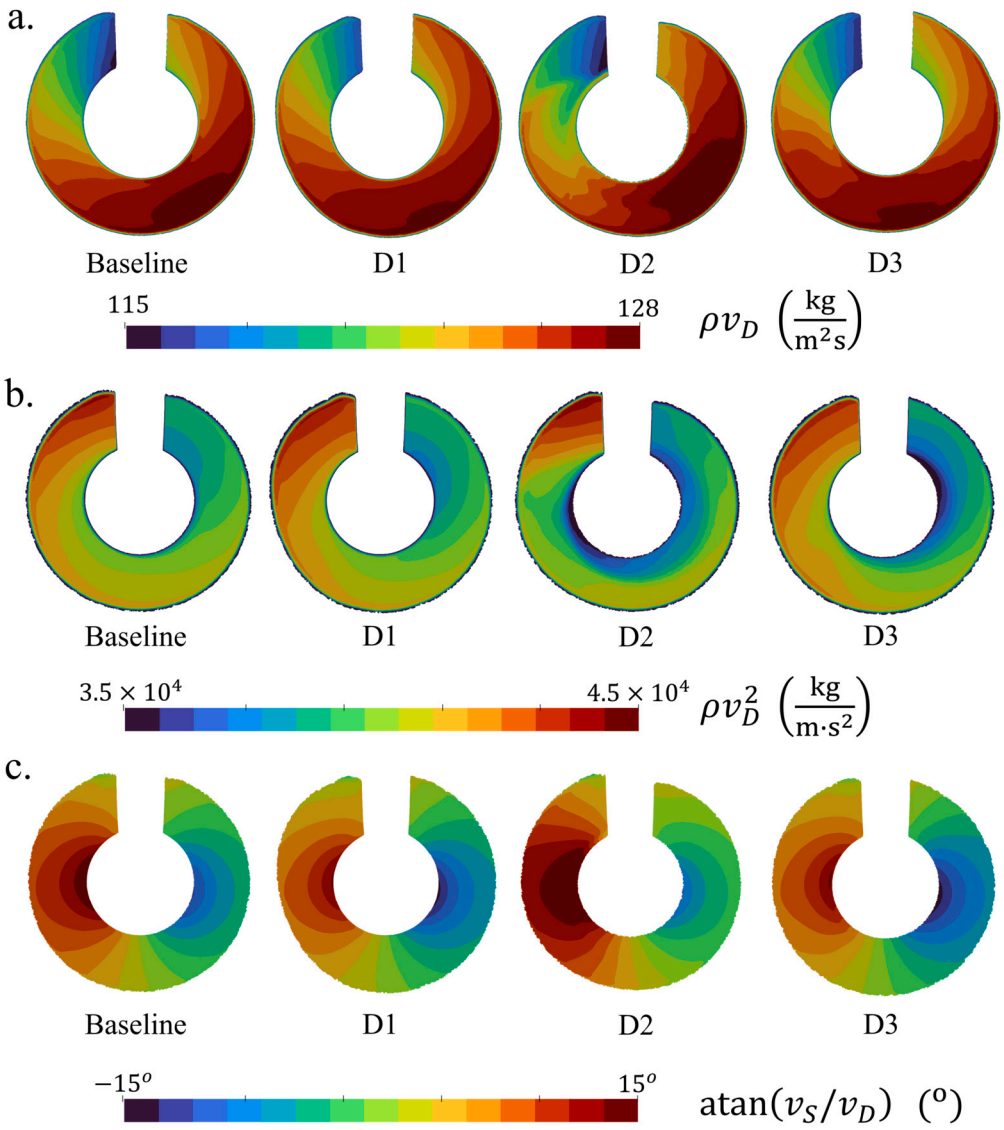


Fig. 19. (a) Mass flux (ρv_D), (b) momentum flux (ρv_D^2) and (c) lateral flow angle ($atan(v_S/v_D)$) distributions inside the bypass jet for the baseline configuration and non-axisymmetric exhausts (D1, D2, D3). The planes are $1m$ downstream of the bypass nozzle exit.

4. Conclusions

This research presents a design exploration and optimisation methodology for installed ultra-high bypass ratio aero-engines with non-axisymmetric exhausts. The method combines a fully parametric approach for the characterisation of 3D exhaust configurations with design and optimisation methods based on Euler CFD and response surface modelling. The approach identified designs that could potentially benefit the aircraft net vehicle force by up to $\Delta NVF = 0.007 F_N$ when assessed with viscous CFD, relative to an axisymmetric baseline. This is approximately a reduction of 0.7% in cruise fuel burn for a close coupled configuration.

Overall, this work has demonstrated that non-axisymmetric exhausts can benefit the overall aircraft net vehicle force. These designs should target the optimisation of the NVF rather than exclusively optimizing propulsive metrics. The latter might lead to penalties at aircraft level due to increased drag. In addition, it was found that the shear perturbation of the bypass nozzle (ψ_A, θ_A) is the dominant design feature. Moreover, non-axisymmetric exhausts should be configured with inboard sheared bypass nozzles and locally reduced trailing edge radius at the inboard side to maximise the overall benefits of the combined system. The governing aerodynamic mechanisms include a non-axisymmetric expansion of the bypass flow and a reduction of the inboard shocks.

Declaration of competing interest

The authors declare that they have no known competing financial interests or personal relationships that could have appeared to influence the work reported in this paper.

Data availability

The data that has been used is confidential.

Acknowledgements

This work has been funded by Rolls Royce plc and Cranfield University.

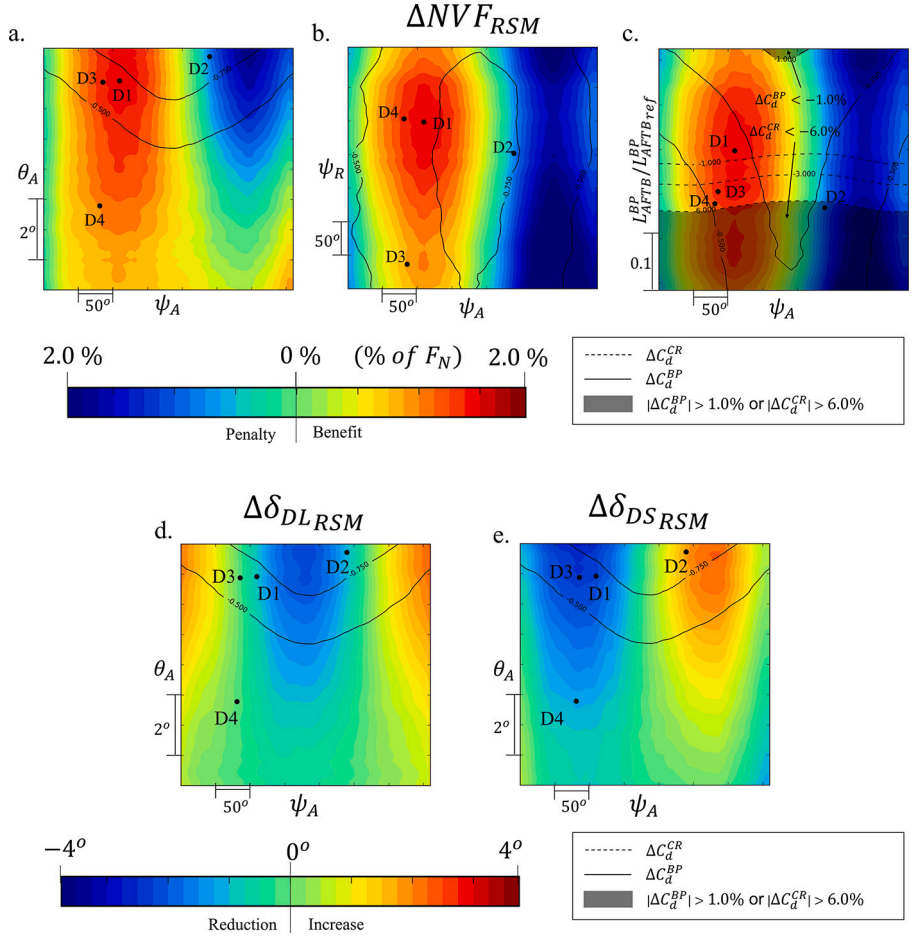


Fig. 20. (a-c) Sensitivity maps of the net vehicle force (ΔNVF), (d) of the vertical ($\Delta\delta_{DL}$) and (e) lateral ($\Delta\delta_{DS}$) thrust vector angles. Shaded areas are where the limits on ΔC_d^{BP} and ΔC_d^{CR} are breached.

References

[1] N.T. Brich, Vision: the prospects for large civil aircraft propulsion, Aeronaut. J. 104 (1038) (2020) 347–352, https://doi.org/10.1017/S0001924000063971.

[2] F. Haselbach, Next generation of large civil aircraft engines-concepts & technologies, in: 11 European Conference on Turbomachinery Fluid Dynamics & Thermodynamics, Madrid, Spain, 2015.

[3] D.L. Berry, The boeing 777 engine/aircraft integration aerodynamic design process, in: ICAS Congress 1994, No ICAS-94-6.4.4, Anaheim, CA, 1994, pp. 1305–1320.

[4] A. Stuermer, DLR TAU-code uRANS turbofan modeling for aircraft aerodynamics investigations, Aerosp. 6 (2019) 121, https://doi.org/10.3390/aerospace6110121, https://www.mdpi.com/2226-4310/6/11/121.

[5] A. Magrini, E. Benini, Aeropropulsive assessment of engine installation at cruise for UHBPR turbofan with body force fan modelling, Aerosp. Sci. Technol. 132 (2023) 108048, https://doi.org/10.1016/j.ast.2022.108048, https://linkinghub.elsevier.com/retrieve/pii/S1270963822007222.

[6] I. Goulos, J. Otter, F. Tejero, J. Hueso-Rebassa, D. MacManus, C. Sheaf, Civil turbofan propulsion aerodynamics: thrust-drag accounting and impact of engine installation position, Aerosp. Sci. Technol. 111 (2021) 106533, https://doi.org/10.1016/j.ast.2021.106533.

[7] A. Magrini, D. Buosi, E. Benini, Analysis of installation aerodynamics and comparison of optimised configuration of an ultra-high bypass ratio turbofan nacelle, Aerosp. Sci. Technol. 128 (2022) 107756, https://doi.org/10.1016/j.ast.2022.107756, https://linkinghub.elsevier.com/retrieve/pii/S1270963822004308.

[8] J. Hueso-Rebassa, F. Tejero, J. Otter, I. Goulos, D. MacManus, Multi-fidelity assessment of exhaust systems for complete engine-aircraft configurations, in: Proceedings of Aerospace Europe Conference 2020 (AEC2020), 00337, Bordeaux, France, 2020.

[9] R. Dun, Scarf Nozzle for a Jet Engine and Method of Using the Same, 2004, United States Patent, Pub. no. US 2004/0140397 A1.

[10] J.J. Otter, R. Christie, I. Goulos, D.G. MacManus, N. Grech, Parametric design of non-axisymmetric separate-jet aero-engine exhaust systems, Aerosp. Sci. Technol. 93 (2019), https://doi.org/10.1016/j.ast.2019.05.038.

[11] J.J. Otter, I. Goulos, R. Christie, D.G. MacManus, Design and analysis of non-axisymmetric installed aero-engine exhaust systems, Aerosp. Sci. Technol. 106 (2020), https://doi.org/10.1016/j.ast.2020.106210.

[12] D. Munday, M. Mihaescu, E. Gutmark, Experimental and numerical study of jets from elliptic nozzles with conic plug, AIAA J. 49 (2011) 554–564, https://doi.org/10.2514/1.J050587.

[13] B. Kulfan, J. Bussoletti, Fundamental parameteric geometry representations for aircraft component shapes, in: 11th AIAA/ISSMO Multidisciplinary Analysis and Optimization Conference, vol. 1, American Institute of Aeronautics and Astronautics, Portsmouth, Virigina, 2006, pp. 547–591.

[14] B. Kulfan, Recent extensions and applications of the 'CST' universal parametric geometry representation method, Aeronaut. J. 114 (1153) (2010) 157–176, https://doi.org/10.1017/S0001924000003614.

[15] R. Christie, A. Heidebrecht, D. MacManus, An automated approach to nacelle parameterization using intuitive class shape transformation curves, J. Eng. Gas Turbines Power 139 (2017), https://doi.org/10.1115/1.4035283.

[16] S. Bagy, M. Lallia, P. Coat, B. Mohammadi, M. Méheut, Aerodynamic shape optimization of aircraft engine nozzles based on computer-aided design, in: AIAA Scitech 2020 Forum, AIAA 2020-2247, American Institute of Aeronautics and Astronautics Inc, AIAA, Orlando, Florida, 2020.

[17] D.G. Krige, A statistical approach to some basic mine valuation problems on the Witwatersrand, J. South. Afr. Instit. Min. Metall. 52 (6) (1951) 119–139.

[18] A.I. Forrester, A.J. Keane, Recent advances in surrogate-based optimization, Prog. Aerosp. Sci. 45 (2009) 50–79, https://doi.org/10.1016/j.paerosci.2008.11.001.

[19] L. He, W. Qian, T. Zhao, Q. Wang, Multi-fidelity aerodynamic data fusion with a deep neural network modeling method, Entropy 22 (2020) 1022, https://doi.org/10.3390/e22091022.

[20] A. Dongare, R.R. Kharde, A.D. Kachare, Introduction to artificial neural network, Int. J. Eng. Innov. Technol. 2 (2012) 189–194.

[21] S. Skinner, H. Zare-Behtash, State-of-the-art in aerodynamic shape optimisation methods, Appl. Soft Comput. 62 (2018) 933–962, https://doi.org/10.1016/j.asoc.2017.09.030.

[22] P. Kupijai, D. Bestle, P.M. Flassig, D. Kickenweitz, Automated multi-objective optimization process for preliminary engine design, in: ASME Turboexpo 2012, Volume 1: Aircraft Engine, Ceramics, Coal, Biomass and Alternative Fuels, Controls, Diagnostics and Instrumentation, American Society of Mechanical Engineers, Copenhagen, Denmark, 2012, pp. 87–96.

[23] F. Tejero, D.G. MacManus, C. Sheaf, Surrogate-based aerodynamic optimisation of compact nacelle aero-engines, Aerosp. Sci. Technol. 93 (2019), https://doi.org/10.1016/j.ast.2019.05.059.
[24] F. Tejero, R. Christie, D. MacManus, C. Sheaf, Non-axisymmetric aero-engine nacelle design by surrogate-based methods, Aerosp. Sci. Technol. 117 (2021), https://doi.org/10.1016/j.ast.2021.106890.
[25] A. Magrini, D. Buosi, E. Benini, Maximisation of installed net resulting force through multi-level optimisation of an ultra-high bypass ratio engine nacelle, Aerosp. Sci. Technol. 119 (2021) 107169, https://doi.org/10.1016/j.ast.2021.107169, https://linkinghub.elsevier.com/retrieve/pii/S1270963821006799.
[26] I. Goulos, J.J. Otter, T. Stankowski, D. MacManus, N. Grech, C. Sheaf, Aerodynamic design of separate-jet exhausts for future civil aero-engines - part II: design space exploration, surrogate modeling, and optimization, J. Eng. Gas Turbines Power 138 (2016), https://doi.org/10.1115/1.4032652.
[27] I. Goulos, J. Otter, T. Stankowski, D. MacManus, N. Grech, C. Sheaf, Design optimisation of separate-jet exhausts for the next generation of civil aero-engines, Aeronaut. J. 122 (2018) 1586–1605, https://doi.org/10.1017/aer.2018.95.
[28] S. Smith, M. Nemec, S. Krist, Integrated nacelle-wing shape optimization for an ultra-high bypass fanjet installation on a single-aisle transport configuration, in: 51st AIAA Aerospace Sciences Meeting Including the New Horizons Forum and Aerospace Exposition, AIAA 2013-0543, American Institute of Aeronautics and Astronautics, Dallas, Texas, 2013.
[29] A. Ronzheimer, M. Hepperle, J. Brezillon, O. Brodersen, J. Lieser, Aerodynamic optimal engine integration at the fuselage tail of a generic business jet configuration 121 (2013) 25–32, https://doi.org/10.1007/978-3-642-35680-3_4.
[30] F. Sánchez-Moreno, D. MacManus, J. Hueso-Rebassa, F. Tejero, C. Sheaf, Optimisation of installed compact and robust nacelles using surrogate models, 2022.
[31] I. Goulos, T. Stankowski, D. MacManus, P. Woodrow, C. Sheaf, Civil turbofan engine exhaust aerodynamics: impact of bypass nozzle after-body design, Aerosp. Sci. Technol. 73 (2018) 85–95, https://doi.org/10.1016/j.ast.2017.09.002.
[32] I. Goulos, D. MacManus, C. Sheaf, Civil turbofan engine exhaust aerodynamics: impact of fan exit flow characteristics, Aerosp. Sci. Technol. 93 (2019), https://doi.org/10.1016/j.ast.2019.05.033.
[33] D.W. Levy, K.R. Laflin, E.N. Tinoco, J.C. Vassberg, M. Mani, B. Rider, C.L. Rumsey, R.A. Wahls, J.H. Morrison, O.P. Brodersen, S. Crippa, D.J. Mavriplis, M. Murayama, Summary of data from the fifth computational fluid dynamics drag prediction workshop, J. Aircr. 51 (2014) 1194–1213, https://doi.org/10.2514/1.C032389.
[34] J.C. Vassberg, E.N. Tinoco, M. Mani, B. Rider, T. Zickuhr, D.W. Levy, O.P. Brodersen, B. Eisfeld, S. Crippa, R.A. Wahls, J.H. Morrison, D.J. Mavriplis, M. Murayama, Summary of the fourth AIAA computational fluid dynamics drag prediction workshop, J. Aircr. 51 (2014) 1070–1089, https://doi.org/10.2514/1.C032418.
[35] M. Rivers, A. Dittberner, Experimental investigations of the NASA common research model in the NASA langley national transonic facility and NASA ames 11-ft transonic wind tunnel (invited), in: 49th AIAA Aerospace Sciences Meeting Including the New Horizons Forum and Aerospace Exposition, AIAA 2011-1126, American Institute of Aeronautics and Astronautics, Orlando, Florida, 2011.
[36] M.B. Rivers, A. Dittberner, Experimental investigations of the NASA common research model, J. Aircr. 51 (2014) 1183–1193, https://doi.org/10.2514/1.C032626.
[37] ISO International Standard 2533-1975, Standard Atmosphere First Edition, Tech. Rep., ISO, Geneva, Switzerland, 1978.
[38] I. Goulos, T. Stankowski, J. Otter, D. MacManus, N. Grech, C. Sheaf, Aerodynamic design of separate-jet exhausts for future civil aero-engines - part I: parametric geometry definition and computational fluid dynamics approach, J. Eng. Gas Turbines Power 138 (2016), https://doi.org/10.1115/1.4032649.
[39] Ansys Inc., ANSYS FLUENT User's Guide, Tech. Rep., 2021.
[40] F.R. Menter, Two-equation eddy-viscosity turbulence models for engineering applications, AIAA J. 32 (8) (1994) 1598–1605.
[41] W. Sutherland, The viscosity of gases and molecular force, Philos. Mag. Ser. 5 36 (1893) 507–531.
[42] I.B. Celik, U. Ghia, P.J. Roache, C.J. Freitas, H. Coleman, P.E. Raad, Procedure for estimation and reporting of uncertainty due to discretization in CFD applications, J. Fluids Eng. 130 (2008) 078001, https://doi.org/10.1115/1.2960953.
[43] K.L. Mikkelsen, D.J. Myren, D.G. Dahl, M. Christiansen, Initial subscale performance measurements of the AIAA dual separate flow reference (DSFR) nozzle, in: AIAA Propulsion and Energy Forum, 51st AIAA/SAE/ASEE Joint Propulsion Conference, AIAA2015-3883, American Institute of Aeronautics and Astronautics, Orlando, Florida, 2015.
[44] AGARD, Aerodynamics of Power Plant Installation, Tech. Rep., 1981.
[45] J. Vassberg, M. Dehaan, M. Rivers, R. Wahls, Development of a common research model for applied CFD validation studies, in: 26th AIAA Applied Aerodynamics Conference, AIAA 2008-6919, American Institute of Aeronautics and Astronautics, Honolulu, Hawaii, 2008.
[46] A. Olsson, G. Sandberg, O. Dahlblom, On Latin hypercube sampling for structural reliability analysis, Struct. Saf. 25 (2003) 47–68, https://doi.org/10.1016/S0167-4730(02)00039-5.
[47] R. Gommers, T.E. Oliphant, M. Haberland, T. Reddy, D. Cournapeau, E. Burovski, P. Peterson, W. Weckesser, J. Bright, S.J. van der Walt, M. Brett, J. Wilson, K.J. Millman, N. Mayorov, A.R.J. Nelson, E. Jones, R. Kern, E. Larson, C.J. Carey, I. Polat, Y. Feng, E.W. Moore, J. VanderPlas, D. Laxalde, J. Perktold, R. Cimrman, I. Henriksen, E.A. Quintero, C.R. Harris, A.M. Archibald, A.H. Ribeiro, F. Pedregosa, P. van Mulbregt, SciPy 1.0 Contributors, SciPy 1.0: fundamental algorithms for scientific computing in python, Nat. Methods 17 (2020) 261–272, https://doi.org/10.1038/s41592-019-0686-2.
[48] R. Kohavi, A study of cross-validation and bootstrap for accuracy estimation and model selection, in: Proceedings of the 14th International Joint Conference on Artificial Intelligence, vol. 2, Morgan Kaufmann Publishers Inc., San Francisco, CA, USA, 1995, pp. 1137–1143.
[49] A. Tonda, Inspyred: bio-inspired algorithms in python, Genet. Program. Evol. Mach. 21 (2020) 269–272, https://doi.org/10.1007/s10710-019-09367-z.



https://dspace.org/

Design optimisation of non-axisymmetric exhausts for installed civil aero-engines

Hueso Rebassa, Josep; MacManus, David G.; Tejero, Fernando; Goulos, Ioannis; Sánchez-Moreno, Francisco ...

2023-11-01
Elsevier
https://doi.org/10.1016/j.ast.2023.108700
Hueso-Rebassa J, MacManus D, Tejero F, et al., (2023) Design optimisation of non-axisymmetric exhausts for installed civil aero-engines. Aerospace Science and Technology, Volume 142, Part B, November 2023, Article Number 108700

Downloaded from a DSpace repository. https://dspace.org/